UC Berkeley

UC Berkeley Electronic Theses and Dissertations

Title

Effects of particle shape and fluid shear on the kinematics and mass transfer of large particles in turbulent flow

Permalink

https://escholarship.org/uc/item/9sw853x8

Author

Oehmke, Theresa B

Publication Date

2021

Peer reviewed|Thesis/dissertation

Effects of particle shape and fluid shear on the kinematics and mass transfer of large
particles in turbulent flow

by

Theresa B. Oehmke

A dissertation submitted in partial satisfaction of the

requirements for the degree of

Doctor of Philosophy

in

Engineering - Civil & Environmental Engineering

in the

Graduate Division

of the

University of California, Berkeley

Committee in charge:

Professor Evan A. Variano, Chair
Associate Professor Laurel Larsen
Assistant Professor Simo A. Mäkiharju

Summer 2021

Effects of particle shape and fluid shear on the kinematics and mass transfer of large particles in turbulent flow

Abstract

Effects of particle shape and fluid shear on the kinematics and mass transfer of large
particles in turbulent flow

by

Theresa B. Oehmke

Doctor of Philosophy in Engineering - Civil & Environmental Engineering

University of California, Berkeley

Professor Evan A. Variano, Chair

In this dissertation I set out to determine how shape and size influence the kinematics and mass flux of Taylor-lengthscale-sized particles in homogeneous isotropic turbulence. Through laboratory experiments, I investigated different sized and shaped flat particles to determine what happens with the spinning and tumbling of those particles in turbulent environments. The results of this first set of experiments showed dependence of particle spinning and tumbling on particle size, but not shape. The size-dependent results from the flat particles agreed with the findings for fibers Oehmke, Bordoloi, et al. 2021 and cuboids Pujara et al. 2018.

To determine the mass flux of Taylor-lengthscale-sized particles, I developed a new particle to study dissolution in turbulence. This particle was made from a sugar-glass recipe and had the characteristics of being neutrally buoyant and shape-similar while it dissolved Oehmke and E. A. Variano 2021. Based on results from previous work that characterized motion Pujara et al. 2018; Bordoloi and E. Variano 2017; Byron et al. 2015, I created rod- and disc-like particles and compared their surface area, volume, and surface-area-to-volume ratios. In all cases, the disc-shaped particles dissolved faster than the rod-shaped particles signifying that shape plays an important role in dissolution dynamics.

To My Grandmother, Geraldine James, thanks for always inspiring confidence.

Get it, Girl!

And to my Grandma Hiya, my namesake. Thanks for trailblazing for me.

Contents

List of Figures

List of Tables

List of Symbols

A	cross-sectional area
C	concentration
d_{eq}	sphere-equivalent diameter
$\mathcal{D}_i$	diffusivity coefficient in i-direction
ϵ	rate of energy dissipation per unit mass
η	Kolmogorov lengthscale
J_i	Flux in i-direction
k	mass transfer coefficient
k_w	wavenumber
L_I	integral lengthscale
λ_T	Taylor microscale
M	mass
M_4^*	normalized 4th moment
ν	kinematic viscosity of a fluid
Ω_s	spinning rate vector
Ω_t	tumbling rate vector
p_x	particle x-vector aligned with shape vertex
p_y	particle y-vector
p_z	particle z-vector perpendicular to particle plane
Re	Reynolds number
$\boldsymbol{R}$	Rotation matrix
ρ	density
$S(t)$	particle trajectory at time t
T	Translation vector
τ_k	Kolmogorov timescale
τ_0	zero-crossing time
u_i	velocity in i-direction
u_i'	turbulent velocity fluctuation in i-direction
$\langle u_i'C'\rangle$	turbulent mass flux in i-direction
u_r	eddy turnover rate at size r
V	volume
x_i	position in i-direction

Acknowledgments

A PhD is like standing on the edge of a cliff in the dark, and then someone pushes you off. These are the words my advisor, Evan Variano, said to me when we first discussed what it was like to do research at a PhD level. Somehow I convinced him that I was capable of that work, and now here you are, reading my dissertation.

When I started this journey, I had no idea what I wanted to do afterward. I was sure of only one thing: with a PhD came a cool gown, and I really wanted that. I also knew that I wanted to have the choice to lead my own projects and do things no one had ever done before. I loved mentoring even before I came to grad school, but somewhere along the way I discovered the joy of teaching and leading people out of the clouds of confusion that can accompany learning a new skill. In these acknowledgements I hope to show even a glimmer of the gratitude I feel towards those who poked holes into the darkness that surrounded me as I struggled to reorient myself after I fell.

I would first like to thank my advisor, Evan Variano, who kept me on track with my research no matter how many detours I tried to take. Through our conversations both about research and about life, I have grown so much as a person and a researcher. There are too many details to put in words here, but I would like to say thank you for all of your support.

I would also like to thank all of my committee members from my preliminary exam through my qualifying exam and onto my dissertation: Sally Thompson, Mark Stacey, Markita Landry, Simo Makiharju, and Laurel Larsen.

To my environmental fluid mechanics and hydrology (EFMH) family at Berkeley and across the country, thank you so much for your support inside and outside of the lab. A special shout out to Nimish Pujara for answering the same question roughly one thousand different ways as I studied for my prelim exam and to Maddie Foster-Martinez for helping me parse through what it means to be a PhD student in all the various phases. Of course I cannot forget all of my office and lab members and all of the international scholars who visited during my time. Included in this family are my wonderful undergrads, without whom I would not have the data to present this dissertation. Tracy Shearer, Bond Bortman, Derek Morimoto, and Jennifer Almendarez I wish you the best as you pursue graduate school and your professional endeavors. I could not have done any of this without you.

Even though the EFMH community across the country is small, it still took me a few years to meet some of the researchers at other institutions. I can trace some of my first introductions into the general EFMH community to Blair Johnson. Blair, I am so fortunate to have you as a mentor and a colleague as I take my next steps in this field.

One of the defining experiences of my graduate school career is the time I spent in Marseille, France. I cannot express enough the gratitude and appreciation I feel toward the entire research community at Institute de Recherche pour les Phénomènes Hors Equilibres (IRPHE). I feel lucky to have been advised by Gautier Verhille and to have been taken in by his whole team. I learned so much about different ways of approaching research questions and designing an individual research philosophy. My office-mates, Amélie Gay and Florian Brunier-Coulin, were the best one could have hoped for and I'm thankful for all of the help

they gave me and all of the Franglais they suffered through in my attempts at communication. My time in lab would not have been the same without the help and company of Christophe B., Sihem B. and all of the other doctoral students, post-docs, researchers, and staff at IRPHE.

Similar to fluid taking the shape of the container that holds it, fluid mechanics research has no set boundaries and spans many departments. I would be remiss to not acknowledge the Mechanical Engineers who adopted me and helped with all aspects of my turbulence education. Eric Ibarra, Shuangjiu Fu, Daniel Grieb, and Abdullah Kuraan thank you for being my extra set of hands in lab, helping me through the strenuous process of downloading the correct software for analysis, and for making me take long lunch breaks in the sunshine.

My time at Berkeley wouldn't be the same without all of the groups and activities I participated in and the people who made those groups so special: Women's Club Water Polo, Master's Swimming, EWOCC, BGESS and everyone in my MS Cohort.

There are, of course, people who don't fit into the neatly defined categories above. My housemates Aron G., Diana H., and Bavisha K., who dealt with me during some of the most stressful times of PhD. Shanasia S. and Marisa F. who have been there for me since undergrad, and without whom I may never have finished undergrad let alone grad school. I'd like to thank Spiderman, whose interest in topology has hitherto been inimical to his crime fighting abilities. And all the others who have checked-in with me, visited, called, and generally supported me throughout the years including, but not limited to, Raul B., Kayla H., Abraham G., Genna S., Shelby W., Jessica R., Gracie D., and the Wolfpack.

Finally, thank you most of all to my family. My parents Patty and Jim Oehmke who have read over various drafts of this document, visited me in all parts of the world, and generally supported my academic pursuits. My sister, Alex, who will always remind me that just because you study, that doesn't make you smart. And my extended family, my aunt and uncle, my grandparents, and my cousins who have provided words of encouragement and support throughout this whole journey.

Chapter 1

Motivation

The study of turbulent flows and objects within them (such as small ocean organisms, debris, atmospheric particles, etc) is a broad and complicated field with many industrial and environmental applications. Industries such as pharmaceutics, paper making, food and cosmetics processing plants, and oil refineries depend on detailed understandings of mixing, settling, and dissolution to achieve reproducibility in their desired outcome. In the environment, the ocean and atmosphere are full of turbulence, transport, and mixing; investigating these natural processes is important for our overall understanding of multiphase flows, stratified flow, life below water, urban flows for sustainability, and weather and climate modeling Dauxois et al. 2021.

Many industries where dissolving and mixing is important use turbulence to aid in that process. Relevant examples include dissolving particles in a reactor Boon-Long, Laguerie, and Couderc 1978; Sano, Yamaguchi, and Adachi 1974, optimizing drug delivery Shah and Nelson 1975; Grijseels, Crommelin, and Blaey 1981; Polli et al. 1997, and determining how paper fibers settle Lundell, Söderberg, and Alfredsson 2011. Similar examples occur in the environment when looking at how seeds settle out of the water column Follett, Hays, and Nepf 2019, or how ice crystals fall from clouds Podzimek 1969; Sassen 1980. Not only is motion important, but in many environments researchers are concerned about solute transport to and from objects such as planktonic (drifting) organisms Nishihara and Ackerman 2007; Kiørboe and Saiz 1995. In special cases such as navigation, suspended mini-robots are able to move themselves Willis 2008; Bruhn et al. 2005.

Importantly, in many of the examples given above, the size and shape of the objects relative to the flow properties is one of the defining characteristics. Many of the example objects are not spherical. This anisotropy brings in additional complexities to the problem.

My area of interest is to understand broadly how non-spherical objects (particles) interact with their environment, but more specifically how the dynamics of particle motion can impact the transport of particles and the transport of mass near a particle surface. Within this field of study, size is important both to model what sized particles are found naturally, and because the equations of motion and the forces acting on particles differ based on particle size.

To this extent, I focus on particles within an area of turbulence called the inertial subrange (see chapter 2.1) and explore their behavior experimentally. Fibers, ellipsoids, and cuboids have already been characterized, and these results show that while they all follow a similar scaling law, the dominant dimension for motion changes depending on the shape Byron et al. 2015; Bordoloi and E. Variano 2017; Pujara et al. 2018; Oehmke, Bordoloi, et al. 2021. For example, for fibers, the dominant dimension for tumbling is the fiber length, however, the dominant dimension for spinning is the fiber diameter Oehmke, Bordoloi, et al. 2021. For cuboids, where spinning and tumbling were not decomposed, the dominant dimension for the overall motion is the volume equivalent diameter Pujara et al. 2018.

To complement the existing knowledge in the field, I work to shrink the gap in research surrounding the behavior of flat, disc-like particles. Discs are oftentimes used as an idealized shape to model snowflakes, ice crystals, leaves, diatoms, red blood cells, etc. In this work, I determine whether discs are a valid simplification for anisotropic flat particles. In chapter 3 I introduce the Kolmogorov microscale normalized circumscribed diameter as the relevant parameter dictating the motion of flat particles, regardless of shape. Having answered the question of how shape and size influence particle motion, we can suggest simplified shapes to model complex objects.

Based on information about scaling laws from previous studies Byron et al. 2015; Bordoloi and E. Variano 2017; Pujara et al. 2018 I also introduce, to my knowledge, the first experimental study addressing dissolving and free-moving anisotropic particles. Chapter 4 discusses the method I developed for creating the particles of interest and chapter 5 introduces a hypothesis about which parameters are important in determining dissolution rate based on shape Oehmke and E. A. Variano 2021. Some of these parameters include the surface-area-to-volume ratio of a particles, which is a common parameter in smaller-scale dissolution experiments Zhang, Werth, and Webb 2002. Rather surprisingly, we note that it is the shape rather than strictly the surface area-to-volume which dictates dissolution for large particles. The set-up of this study allows us to say something about the methods for direct measurement of turbulent mass flux from the dissolving particles as well.

References

Boon-Long, S., C. Laguerie, and J. P. Couderc (1978). "Mass transfer from suspended solids to a liquid in agitated vessels". en. In: *Chemical Engineering Science* 33.7, pp. 813–819. ISSN: 0009-2509. DOI: 10.1016/0009-2509(78)85170-7.

Bordoloi, Ankur D. and Evan Variano (2017). "Rotational kinematics of large cylindrical particles in turbulence". en. In: *Journal of Fluid Mechanics* 815, pp. 199–222. ISSN: 0022-1120, 1469-7645. DOI: 10.1017/jfm.2017.38.

Bruhn, F. C., F. D. Carsey, J. Kohler, M. Mowlem, C. R. German, and A. E. Behar (2005). "MEMS enablement and analysis of the miniature autonomous submersible explorer". In: *IEEE Journal of Oceanic Engineering* 30.1, pp. 165–178. ISSN: 0364-9059. DOI: 10.1109/JOE.2004.836420.

Byron, M., J. Einarsson, K. Gustavsson, G. Voth, B. Mehlig, and E. Variano (2015). "Shape-dependence of particle rotation in isotropic turbulence". en. In: *Physics of Fluids* 27.3, p. 035101. ISSN: 1070-6631, 1089-7666. DOI: 10.1063/1.4913501.

Dauxois, T., T. Peacock, P. Bauer, C. P. Caulfield, C. Cenedese, C. Gorlé, G. Haller, G. N. Ivey, P. F. Linden, E. Meiburg, N. Pinardi, N. M. Vriend, and A. W. Woods (2021). "Confronting Grand Challenges in environmental fluid mechanics". In: *Physical Review Fluids* 6.2, p. 020501. DOI: 10.1103/PhysRevFluids.6.020501.

Follett, Elizabeth, Cynthia G. Hays, and Heidi Nepf (2019). "Canopy-Mediated Hydrodynamics Contributes to Greater Allelic Richness in Seeds Produced Higher in Meadows of the Coastal Eelgrass Zostera marina". English. In: *Frontiers in Marine Science* 6. ISSN: 2296-7745. DOI: 10.3389/fmars.2019.00008.

Grijseels, H., D. J. A. Crommelin, and C. J. de Blaey (1981). "Hydrodynamic approach to dissolution rate". en. In: *Pharmaceutisch weekblad* 3.1, pp. 1005–1020. ISSN: 0031-6911, 1573-739X. DOI: 10.1007/BF02193318.

Kiørboe, T and E Saiz (1995). "Planktivorous feeding in calm and turbulent environments, with emphasis on copepods". en. In: *Marine Ecology Progress Series* 122, pp. 135–145. ISSN: 0171-8630, 1616-1599. DOI: 10.3354/meps122135.

Lundell, Fredrik, L. Daniel Söderberg, and P. Henrik Alfredsson (2011). "Fluid Mechanics of Papermaking". In: *Annual Review of Fluid Mechanics* 43.1, pp. 195–217. DOI: 10.1146/annurev-fluid-122109-160700.

Nishihara, Gregory N. and Josef D. Ackerman (2007). "On the determination of mass transfer in a concentration boundary layer". en. In: *Limnology and Oceanography: Methods* 5.2, pp. 88–96. ISSN: 1541-5856. DOI: https://doi.org/10.4319/lom.2007.5.88.

Oehmke, Theresa B., Ankur D. Bordoloi, Evan Variano, and Gautier Verhille (2021). "Spinning and tumbling of long fibers in isotropic turbulence". In: *Physical Review Fluids* 6.4, p. 044610. DOI: 10.1103/PhysRevFluids.6.044610.

Oehmke, Theresa B. and Evan A. Variano (2021). "A new particle for measuring mass transfer in turbulence". en. In: *Experiments in Fluids* 62.1, p. 16. ISSN: 1432-1114. DOI: 10.1007/s00348-020-03084-5.

Podzimek, Josef (1969). "Contribution to the explanation of the motion of a falling column-like ice crystal". en. In: *Studia Geophysica et Geodaetica* 13.2, pp. 199–206. ISSN: 0039-3169, 1573-1626. DOI: 10.1007/BF02587821.

Polli, James E., G. Singh Rekhi, Larry L. Augsburger, and Vinod P. Shah (1997). "Methods to compare dissolution profiles and a rationale for wide dissolution specifications for metoprolol tartrate tablets". en. In: *Journal of Pharmaceutical Sciences* 86.6, pp. 690–700. ISSN: 1520-6017. DOI: 10.1021/js960473x.

Pujara, Nimish, Theresa B. Oehmke, Ankur D. Bordoloi, and Evan A. Variano (2018). "Rotations of large inertial cubes, cuboids, cones, and cylinders in turbulence". en. In: *Physical Review Fluids* 3.5. ISSN: 2469-990X. DOI: 10.1103/PhysRevFluids.3.054605.

Sano, Yuji, Nobutaka Yamaguchi, and Toshiro Adachi (1974). "Mass Transfer Coefficients for Suspended Particles in Agitated Vessels and Bubble Columns". In: *Journal of Chemical Engineering of Japan* 7.4, pp. 255–261. DOI: 10.1252/jcej.7.255.

Sassen, Kenneth (1980). "Remote Sensing of Planar Ice Crystal Fall Attitudes". en. In: *Journal of the Meteorological Society of Japan. Ser. II* 58.5, pp. 422–429. ISSN: 0026-1165, 2186-9057. DOI: 10.2151/jmsj1965.58.5_422.

Shah, Ashok C. and Kenneth G. Nelson (1975). "Evaluation of a convective diffusion drug dissolution rate model". en. In: *Journal of Pharmaceutical Sciences* 64.9, pp. 1518–1520. ISSN: 1520-6017. DOI: 10.1002/jps.2600640920.

Willis, Mark A. (2008). "Chemical Plume Tracking Behavior in Animals and Mobile Robots". en. In: *Navigation* 55.2, pp. 127–135. ISSN: 2161-4296. DOI: 10.1002/j.2161-4296.2008.tb00423.x.

Zhang, Changyong, Charles J. Werth, and Andrew G. Webb (2002). "A Magnetic Resonance Imaging Study of Dense Nonaqueous Phase Liquid Dissolution from Angular Porous Media". en. In: *Environmental Science & Technology* 36.15, pp. 3310–3317. ISSN: 0013-936X, 1520-5851. DOI: 10.1021/es011497v.

Chapter 2

Background

In this chapter I hope to introduce some of the general concepts that will be discussed in this dissertation. My aim is to explain the various components that contribute to orientation and rotation kinematics in turbulent flow as well as give background on turbulent mass flux, which is explored during the shape-motion-flux experiments (Chapter 5.3).

2.1 Turbulence

There are many ways to think about turbulence in fluids. One popular approach is to think about a flow's energy spectrum, thus taking a spectral analysis approach. Sometimes this is the most appropriate method for analyzing fluids, but not necessarily the most intuitive way. A more intuitive approach could stem from observing turbulent structures and contextualizing them within the typical behavior of generic turbulent flows.

Turbulent flows in general develop from instabilities. These instabilities typically evolve from some type of fluid shear (layers of fluid moving past each other at different rates) mixed with a perturbation. A common example in open channel flow is when high-speed laminar flow goes over some type of bump in the bed. The flow develops an instability, and has enough energy that the viscous forces cannot dampen the instability back down to laminar flow. When this happens, the instability grows until it breaks apart and turbulent flow forms.

There are several common characteristics of turbulent flow.

1. A high Reynolds number $Re = UL/\nu$, where U and L are characteristic velocity- and length-scales, respectively, and ν is the kinematic viscosity of the fluid in $[L^2/T]$. For turbulent Reynolds numbers, turbulent velocity fluctuations, u', are often used as the characteristic velocity-scale.

2. Chaotic, unsteady, and unpredictable velocity and pressure

3. A wide range of scales and motion where the largest scales are determined by the domain and the smallest scales are determined by the rate of energy dissipation, ϵ, and
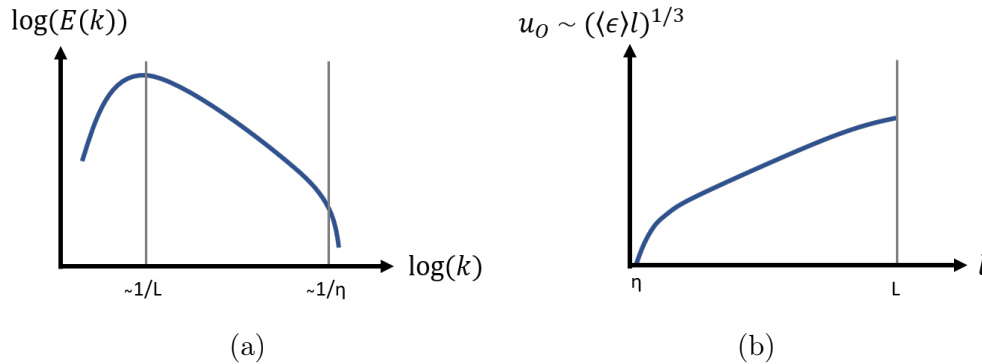
Figure 2.1: (a) A power-spectrum perspective on turbulent kinetic energy based on wavenumber, k_w. (b) A scaling perspective on turbulent energy. Here L is the size of the largest energy containing eddies and η is the Kolmogorov microscale. At scale smaller than η viscous dissipation dominates. The vertical lines bound the inertial subrange of turbulence.

the kinematic viscosity ν. Using scaling analysis, the smallest lengthscale of turbulence, the Kolmogorov scale η can be composed from ν and ϵ as $\eta = \left(\frac{\nu^3}{\epsilon}\right)^{1/4}$.

4. Quickly mixed scalars and momentum

5. Flow with vorticity (e.g., the flow spins)

6. Three-dimensional flow patterns

Large Reynolds numbers, as described above, are one of the most fundamental aspects of turbulent flow. The Reynolds number is non-dimensional and shows the ratio of inertial forces to viscous forces. The value of the Reynolds number at which turbulent flow initiates depends on the system of interest. For many systems the 'transition to turbulence' begins with a Reynolds number of 2000 to 10000 or greater, showing that inertial forces dominate over viscous forces.

A high Reynolds number is necessary for some of the other characteristics of turbulent flow described above to occur. For example, item number 3 above ('separation of scales') occurs when Re is high enough that the large scales of turbulence are much much bigger than the intermediate scales which are much much bigger than the small, dissipative scales. Kinetic energy in turbulent flow is generally input at the large scales then transferred through smaller and smaller scales until finally it is dissipated to heat energy. This intermediate region is called the inertial subrange, and is where inertial and viscous forces are on the same order of magnitude within turbulent flow. Within this range the rate of energy transferred ($\epsilon \, [L^2/T^3]$) is approximately constant.

Figure 2.1a shows a relationship between the wavenumber of the flow, k_w and the kinetic energy of the flow at the associated wavenumber $E(k_w)$. The wavenumber, $k_w \equiv 2\pi/l$,

measures the spatial frequency and can be thought of as number of cycles per unit distance. Figure 2.1a is commonly known as the turbulent energy cascade. The area with a -5/3 power-law slope between $\sim 1/L$ and $\sim 1/\eta$ marks the intertial subrange of turbulence where energy is transferred from large eddies to smaller and smaller ones at a constant rate until the eddy size reaches η, the Kolmogorov lengthscale, and energy is dissipated through viscosity to heat. Here the highest energy is associated with the largest lengthscales, L, and the smallest wavenumbers, meaning that there are fewer cycles per unit distance when the cycles are large. The smallest amount of energy is seen with the smallest lengthscales η and highest wavenumbers.

In his 1941 paper, A. N. Kolmogorov introduced a concept known commonly today as K41 or K41 theory Kolmogorov 1941. This theory states that in fully developed turbulence the turbulent statistical properties of the flow are universal within the inertial subrange. Kolmogorov then went on to say that small-scale properties in high-Re flow are determined by the kinematic viscosity and the rate of energy dissipation ϵ. From these assumptions, a scaling analysis can be done to find η. The steps in this scaling analysis are as follows.

1. $\nu = [L^2/T]$, kinematic viscosity

2. $\epsilon = [L^2/T^3]$, energy dissipation rate
   kinetic energy, $KE = \frac{1}{2}mu_i^2 \sim u_i^2 \ [L^2/T^2]$ for unit mass
   kinetic energy dissipation per unit time $\sim \frac{KE}{T} \ [L^2/T^3]$

3. $\eta = [L]$, Kolmogorov lengthscale
   $\eta = (\frac{\nu^3}{\epsilon})^{1/4} \rightarrow [(\frac{L^2}{T})^3/(L^2/T^3)]^{1/4} \rightarrow [\frac{L^6/T^3}{L^2/T^3}]^{1/4} \rightarrow [L^4]^{1/4} \rightarrow [L]$

Using the Kolmogorov scaling analysis, we can begin to understand figure 2.1b which uses a similar analysis to find the orbital velocity, $u_O \ [L/T]$, of a single eddy (turbulent motion) of specific length-scale l based on the eddy size and the mean energy dissipation rate of the flow. Here the orbital velocity u_O has units of $[L/T]$ and scales as $(\langle\epsilon\rangle l)^{1/3}$ with units of $[(L^2/T^3)L]^{1/3}$ which simplifies to give $[L/T]$. This says that the eddy with the largest size contains the most velocity.

These turbulent characteristics are superimposed on top of a background flow that can be found by averaging. In order to isolate the turbulent characteristics from the mean flow, we have to decompose the total flow into its mean flow component and its turbulent fluctuation component. Breaking apart these two components is called Reynolds' decomposition of the flow. Let's take a variable ξ_i and Reynolds decompose it into its mean and fluctuating components, $\xi_i = \overline{\xi_i} + \xi_i'$. There are a few characteristics to consider when looking at the mean and fluctuating components. The first is that the fluctuations are seen as random, so the mean of the fluctuations is zero. The second is that the average of the mean is still the mean. Using this as a base, we come up with the following relationships:

1. $\overline{\xi'} = 0$

2. $\overline{\overline{\xi}} = \overline{\xi}$

3. $\overline{\overline{\xi_1}\ \overline{\xi_2}} = \overline{\xi_1}\ \overline{\xi_2}$

4. $\overline{\overline{\xi_1}\ \xi'_2} = 0$

5. $\overline{\xi'_1\ \xi'_2} \neq 0$ (in general)

6. $\overline{\alpha\ \xi_i} = \alpha\ \overline{\xi_i}$, α is a constant

7. $\overline{\xi_1 + \xi_2} = \overline{\xi_1} + \overline{\xi_2}$

These relationships form the basis for how turbulence can be introduced into standard flow equations. One such equation is the continuity equation:

$$\frac{\partial \rho}{\partial t} + \nabla \cdot (\rho \mathbf{u}) = 0 \tag{2.1}$$

which says that the mass cannot be created or destroyed, but instead the change of mass within a system must be equal to the amount of mass entering and leaving the system. For a constant-temperature, incompressible system the density does not change over time or space. With these conditions, equation 2.1 simplifies to:

$$\nabla \cdot \mathbf{u} = 0 \tag{2.2}$$

which states that the divergence of the velocity vector must equal zero.

Introducing turbulence to equation 2.2, requires Reynolds decomposing the velocity vectors, taking the expectation, and eliminating terms equal to zero. The first step is to expand equation 2.2:

$$\frac{\partial u}{\partial x} + \frac{\partial v}{\partial y} + \frac{\partial w}{\partial z} = 0 \tag{2.3}$$

Then apply the Reynolds decomposition

$$\frac{\partial}{\partial x}(\overline{u} + u') + \frac{\partial}{\partial y}(\overline{v} + v') + \frac{\partial}{\partial z}(\overline{w} + w') = 0 \tag{2.4}$$

$$\frac{\partial \overline{u}}{\partial x} + \frac{\partial u'}{\partial x} + \frac{\partial \overline{v}}{\partial y} + \frac{\partial v'}{\partial y} + \frac{\partial \overline{w}}{\partial z} + \frac{\partial w'}{\partial z} = 0 \tag{2.5}$$

The next step is to take the expectation value of the continuity equation. The expectation value (or ensemble average) is a statistical mean value for the variable of interest and is designated by $\langle \cdot \rangle$.

$$\frac{\partial \langle \overline{u} \rangle}{\partial x} + \frac{\partial \langle u' \rangle}{\partial x} + \frac{\partial \langle \overline{v} \rangle}{\partial y} + \frac{\partial \langle v' \rangle}{\partial y} + \frac{\partial \langle \overline{w} \rangle}{\partial z} + \frac{\partial \langle w' \rangle}{\partial z} = 0 \tag{2.6}$$
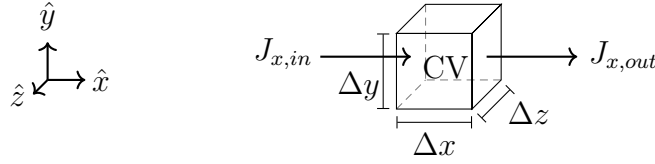
Figure 2.2: Flux in a control volume

Using the properties of mean and fluctuation values described previously, eliminating all terms equal to zero, and taking the mean value to be the expectation value, equation 2.6 reduces to:

$$\frac{\partial \langle u \rangle}{\partial x} + \frac{\partial \langle v \rangle}{\partial y} + \frac{\partial \langle w \rangle}{\partial z} = 0 \tag{2.7}$$

$$\frac{\partial \langle u_i \rangle}{\partial x_i} = 0 \tag{2.8}$$

Equation 2.1 is the Reynolds-averaged continuity equation that will be used in future sections.

2.2 Transport

Most environmental engineers consider transport in terms of pollutants moving through the environment. These pollutant clouds grow and change over time via the fundamental processes of fluid advection and molecular diffusion. The challenge here is to determine exactly how these clouds change over time.

Fluxes

A flux is the transport of something (mass, momentum, heat) across a unit area during a unit timestep. Mass flux, which has units of $[M/TL^2]$, will be discussed in the following examples. In general there are two types of fluxes to consider, advective fluxes and diffusive fluxes. Advective flux is deterministic movement generally due to a velocity field. Diffusive flux is probabilistic and is broadly defined as movement due to random motion.

Starting with a control volume (CV) of volume V with side-lengths $\Delta x, \Delta y, \Delta z$, (pictured in figure 2.2) flux into the CV in the i-direction can be defined as J_i with units of $[M/TL^2]$. Constructing a mass balance of the flux into the CV and the flux out of the CV gives:

$$\frac{\partial M}{\partial t} = (J_{x,in} - J_{x,out})\, \Delta y \Delta z + (J_{y,in} - J_{y,out})\, \Delta x \Delta z + (J_{z,in} - J_{z,out})\, \Delta x \Delta y \tag{2.9}$$
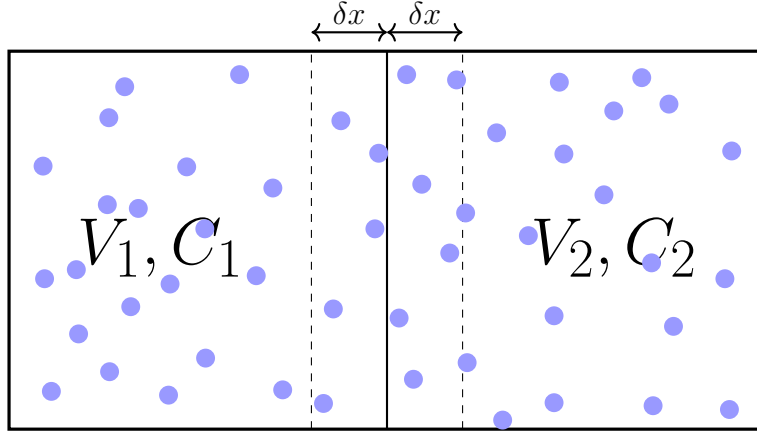
Figure 2.3: Illustration of 1D diffusive flux model. The small dots move $\pm \delta x$ during each timestep with 50% probability.

Then dividing both sides by $\Delta x \Delta y \Delta z$,

$$\frac{1}{\Delta x \Delta y \Delta z}\frac{\partial M}{\partial t} = \frac{(J_{x,in} - J_{x,out})}{\Delta x} + \frac{(J_{y,in} - J_{y,out})}{\Delta y} + \frac{(J_{z,in} - J_{z,out})}{\Delta z} \tag{2.10}$$

$$\frac{\partial C}{\partial t} = \frac{(J_{x,in} - J_{x,out})}{\Delta x} + \frac{(J_{y,in} - J_{y,out})}{\Delta y} + \frac{(J_{z,in} - J_{z,out})}{\Delta z} \tag{2.11}$$

considering an infinitesimally small CV, and applying the definition of a derivative gives an equation for the change in mass in the CV based on the net flux of mass

$$\frac{\partial C}{\partial t} = \frac{-\partial J_x}{\partial x} + \frac{-\partial J_y}{\partial y} + \frac{-\partial J_z}{\partial z} \tag{2.12}$$

$$\frac{\partial C}{\partial t} + \frac{\partial J_i}{\partial x_i} = 0 \tag{2.13}$$

To find the total flux, J_i, we consider its advective and diffusive components, $J_{adv,i}$ and $J_{diff,i}$, respectively. Now we can define the advective flux individually. By definition, $J_{adv,i}$ includes the deterministic velocity component u_i with units of $[L/T]$. The mass for the advective flux comes from the concentration in the system (C $[M/L^3]$) which gives $J_{adv,i} = u_i C$ with units of $[M/T/L^2]$.

Diffusive flux $J_{diff,i}$ can be understood by looking at a simple 1D molecular diffusion model. In this example the dots shown in figure 2.3 can move a distance $\pm \delta x$ with equal probability (the dots do not move vertically). After a timestep of δt half of the dots will have moved $-\delta x$ to the left and half will have moved $+\delta x$ to the right. The dots that hit the left and right boundaries will be contained inside the volume ($V = V_1 + V_2$) and those that move

across the middle boundary will change from volume V_1 to V_2 or the inverse. Concentration C_1 is contained within volume $V_1 = \Delta x \Delta y \Delta z$ and concentration C_2 is contained within volume $V_2 = \Delta x \Delta y \Delta z$.

To determine the diffusive mass flux, we have to turn the concentrations C_1 and C_2 into mass. The amount of mass that has ability to move from V_1 to V_2, $M_{1 \to 2}$, is

$$potential \ M_{1 \to 2} : C_1 \delta x \Delta y \Delta z \tag{2.14}$$

and the amount of mass that has ability to move from V_2 to V_1, $M_{2 \to 1}$ is

$$potential \ M_{2 \to 1} : C_2 \delta x \Delta y \Delta z \tag{2.15}$$

δx is used here because only mass within δx of the border has the potential to cross the middle boundary from V_1 to V_2 or vice versa within a single time-step Δt. Since only half of the mass in $C_1 \delta x \Delta y \Delta z$ and $C_2 \delta x \Delta y \Delta z$ will move into V_2 and V_1 respectively, the amount of mass moving across the border from V_1 to V_2 is

$$actual \ M_{1 \to 2} : \frac{1}{2} C_1 \delta x \Delta y \Delta z \tag{2.16}$$

and the movement across the border from V_2 to V_1 is

$$actual \ M_{2 \to 1} : \frac{1}{2} C_2 \delta x \Delta y \Delta z \tag{2.17}$$

To determine the diffusive flux from $V_1 \to V_2$, we take equation 2.16 and divide by the area it moves through ($A_{border} = \Delta y \Delta z$) and the timestep Δt.

$$J_{diff,x,V_1 \to V_2} = \frac{\frac{1}{2} C_1 \delta x \Delta y \Delta z}{\Delta y \Delta z \Delta t} \tag{2.18}$$

The same is done for the mass moving $M_{2 \to 1}$ to get the flux

$$J_{diff,x,V_2 \to V_1} = -\frac{\frac{1}{2} C_2 \delta x \Delta y \Delta z}{\Delta y \Delta z \Delta t} \tag{2.19}$$

with the negative sign to indicate that the flux is moving in the negative x direction.

With these relationships, we can determine the diffusive flux across the border of the two boxes:

$$J_{diff,x} = \frac{\frac{1}{2} C_1 \delta x \Delta y \Delta z}{\Delta y \Delta z \Delta t} - \frac{\frac{1}{2} C_2 \delta x \Delta y \Delta z}{\Delta y \Delta z \Delta t} \tag{2.20}$$

Simplifying equation 2.20 gives

$$J_{diff,x} = \frac{1}{2} \frac{\delta x}{\Delta t} (C_1 - C_2) \tag{2.21}$$

Next, using a Taylor expansion, C_2 is written in terms of C_1 and the concentration gradient

$$C_2 = C_1 + \delta x \frac{\partial C}{\partial x} + \frac{\delta x^2}{2} \frac{\partial^2 C}{\partial x^2} + \dots \tag{2.22}$$

Plugging in 0th and 1st order terms gives

$$J_{diff,x} = \frac{\delta x}{2\Delta t} \left(C_1 - \left(C_1 + \delta x \frac{\partial C}{\partial x} \right) \right) \tag{2.23}$$

$$= -\frac{\delta x}{2\Delta t} \left(\delta x \frac{\partial C}{\partial x} \right) \tag{2.24}$$

$$= -\left(\frac{\delta x^2}{2\Delta t} \right) \frac{\partial C}{\partial x} \tag{2.25}$$

The generic C represents the continuous concentration profile across the entire volume. The quantity $\left(\frac{\delta x^2}{2\Delta t} \right)$ is the diffusion coefficient $\mathcal{D}_i$ which has a directionality associated with it since it relies on the distance δx a dot can move in the x direction. The distance a dot can move in the other directions δy and δz are not necessarily the same. In the above example $\delta y = \delta z = 0$. Substituting in $\mathcal{D}_i$ gives Fick's first law:

$$J_{diff,i} = -\mathcal{D}_i \frac{\partial C}{\partial x} \tag{2.26}$$

Now that both diffusive and advective fluxes are defined, the total flux can be written as

$$J_i = u_i C - \mathcal{D}_i \frac{\partial C}{\partial x} \tag{2.27}$$

Transport Equation

Once fluxes are understood, we consider pollutant spread by the Transport Equation (also known by many other names such as the convection-diffusion equation, the advection-diffusion equation, and the advection-diffusion-reaction equation). Combining equations 2.13 and 2.27 gives

$$\frac{\partial C}{\partial t} = -\frac{\partial}{\partial x_i} \left(u_i C - \mathcal{D}_i \frac{\partial C}{\partial x} \right) \tag{2.28}$$

Expanding and adding source/sink and reaction terms gives

$$\frac{\partial C}{\partial t} = -\frac{\partial}{\partial x_i} (u_i C) + \frac{\partial}{\partial x_i} \mathcal{D}_i \frac{\partial C}{\partial x_i} + S + R \tag{2.29}$$

Here, the change in concentration, C, of a solute with time, t, is related to the advective flux of the solute, the diffusive flux of the solute, and any sources or sinks and reactions the

solute may have. A source or sink, S, in this case would be any way in which more solute enters or leaves the CV in addition to the two fluxes mentioned above. The reaction, R, may take many different forms including, but not limited to, photochemical reactions, $0th$, $1st$, 2nd etc order chemical reactions, and can represent growth or decay of the concentration C.

To take this equation and apply it to turbulent environments, a turbulent Reynolds decomposition is performed, as described in section 2.1. Velocity and concentration are decomposed as $u_i = \overline{u_i} + u_i'$ and $C = \overline{C} + C'$ respectively, with the overbars denoting the mean values and the prime symbol denoting turbulent fluctuation values. The Reynolds decomposition is substituted into equation 2.29. In this example $S = R = 0$.

$$\frac{\partial(\overline{C} + C')}{\partial t} = -\frac{\partial}{\partial x_i}\left[(\overline{u_i} + u_i')(\overline{C} + C')\right] + \frac{\partial}{\partial x_i}\mathcal{D}_i\frac{\partial(\overline{C} + C')}{\partial x_i} \tag{2.30}$$

Expanding this gives

$$\frac{\partial\overline{C}}{\partial t} + \frac{\partial C'}{\partial t} = -\left[\frac{\partial}{\partial x_i}(\overline{u_i}\,\overline{C}) + \frac{\partial}{\partial x_i}(\overline{u_i}C') + \frac{\partial}{\partial x_i}(u_i'\overline{C}) + \frac{\partial}{\partial x_i}(u_i'C')\right] +$$
$$\frac{\partial}{\partial x_i}\mathcal{D}_i\frac{\partial\overline{C}}{\partial x_i} + \frac{\partial}{\partial x_i}\mathcal{D}_i\frac{\partial C'}{\partial x_i} \tag{2.31}$$

Next, we take the expectation value by ensemble-averaging the whole equation. This is also often known as Reynolds averaging.

$$\frac{\partial\langle\overline{C}\rangle}{\partial t} + \frac{\partial\langle C'\rangle}{\partial t} = -\left[\frac{\partial}{\partial x_i}\langle\overline{u_i}\,\overline{C}\rangle + \frac{\partial}{\partial x_i}\langle\overline{u_i}C'\rangle + \frac{\partial}{\partial x_i}\langle u_i'\overline{C}\rangle + \frac{\partial}{\partial x_i}\langle u_i'C'\rangle\right] +$$
$$\frac{\partial}{\partial x_i}\mathcal{D}_i\frac{\partial\langle\overline{C}\rangle}{\partial x_i} + \frac{\partial}{\partial x_i}\mathcal{D}_i\frac{\partial\langle C'\rangle}{\partial x_i} \tag{2.32}$$

Using the properties shown in section 2.1 the terms equal to zero are eliminated and the mean values are taken to be the expectation values. This leaves

$$\frac{\partial\langle C\rangle}{\partial t} = -\left[\frac{\partial}{\partial x_i}\langle u_iC\rangle + \frac{\partial}{\partial x_i}\langle u_i'C'\rangle\right] + \frac{\partial}{\partial x_i}\mathcal{D}_i\frac{\partial\langle C\rangle}{\partial x_i} \tag{2.33}$$

We can keep going to simplify this transport equation even more by applying the product rule to the terms containing both u_i and C without fluctuations:

$$\frac{\partial\langle C\rangle}{\partial t} = -\left[\langle u_i\rangle\frac{\partial}{\partial x_i}\langle C\rangle + \langle C\rangle\frac{\partial}{\partial x_i}\langle u_i\rangle + \frac{\partial}{\partial x_i}\langle u_i'C'\rangle\right] + \frac{\partial}{\partial x_i}\mathcal{D}_i\frac{\partial\langle C\rangle}{\partial x_i} \tag{2.34}$$

From the turbulent continuity equation 2.8 $\frac{\partial\langle u_i\rangle}{\partial x_i} = 0$ so simplifying gives

$$\frac{\partial\langle C\rangle}{\partial t} = -\left[\langle u_i\rangle\frac{\partial\langle C\rangle}{\partial x_i} + \frac{\partial}{\partial x_i}\langle u_i'C'\rangle\right] + \frac{\partial}{\partial x_i}\mathcal{D}_i\frac{\partial\langle C\rangle}{\partial x_i} \tag{2.35}$$

Rearranging and assuming that diffusivity is constant

$$\frac{\partial \langle C \rangle}{\partial t} + \langle u_i \rangle \frac{\partial \langle C \rangle}{\partial x_i} = \mathcal{D}_i \frac{\partial^2 \langle C \rangle}{\partial x_i^2} - \frac{\partial}{\partial x_i} \langle u_i' C' \rangle \tag{2.36}$$

In equation 2.36 the term $\langle u_i' C' \rangle$ is referred to as the turbulent mass flux. This term is often approximated as a Fickian process where mass moves from an area of high concentration to an area of low concentration, in this case, due to turbulent fluctuations. With these characteristics $\langle u_i' C' \rangle$ can be modelled as a diffusive flux in the form of Fick's first law:

$$\langle u_i' C' \rangle \approx -\mathcal{D}_{turb,i} \frac{\partial \langle C \rangle}{\partial x_i} \tag{2.37}$$

Where $\mathcal{D}_{turb,i}$ is the turbulent diffusivity. One of the major challenges for the 20th and 21st centuries is to model $\mathcal{D}_{turb,i}$ Pope 2000.

2.3 Particles

The goal now is to apply some of these transport concepts to particles in turbulence. One key concept is solute transport from the particle surface to the bulk flow. To figure this out, first we need to understand particle movement (spinning and tumbling) and then link that with solute transport from the particle surface.

Particle Movement

Particle movement can be broken down into two parts, translation and rotation. Translation is fairly straightforward to determine by looking at the change in location of the center of mass of the particle over time. The more complicated part is computing particle rotation. Rotation can be quantified as angular velocity about each axis, or as spinning and tumbling. Spinning is defined as rotation around the particle's symmetry axis, and tumbling is the combined rotation around the other two axes.

An example of the symmetry axis for a flat triangular particle (similar to a disc) is shown in figure 2.4. We define the z-axis as the symmetry axis, so spinning is always around the z-axis. Tumbling is the rotation of the z-axis around the the x- and y- axes. The goal of the analysis detailed in chapter 3 is to determine how the shape and size of a particle influences its spinning and tumbling.

Surface Flux

Transport is typically limited by either diffusive or advective properties. These cases are when either diffusion takes place much quicker than advection, or vice versa. A common way of characterizing which flux dominates transport is to use the Peclet number. The Peclet number, Pe, is the ratio of the advective flux to the diffusive flux in a system.
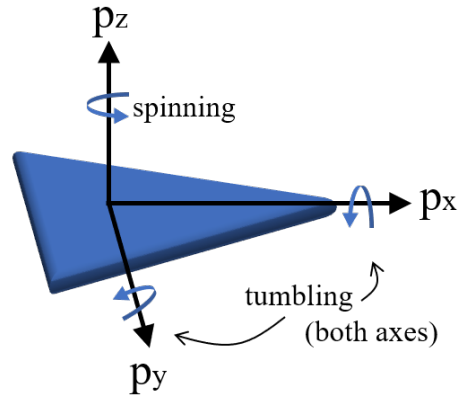
Figure 2.4: Flat triangular particle where the symmetry axis is the z axis.
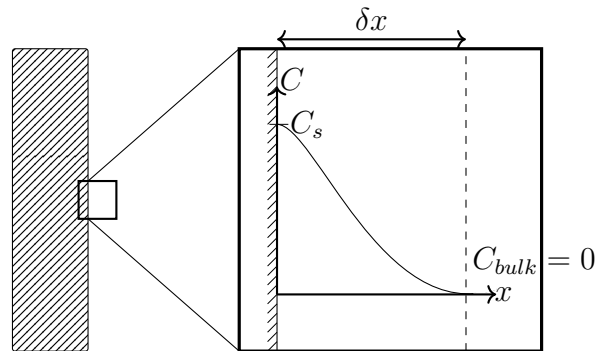
Figure 2.5: Boundary layer close-up of solute coming off of the surface of a particle.

$$Pe = \frac{J_{adv}}{J_{diff}} \tag{2.38}$$

Figure 2.5 shows the system under consideration. The rectangle on the left represents a solid rod-like particle. The close-up shows the boundary layer of that rod which spans δx away from the rod. This is only an example in the $+\hat{x}$ direction, the boundary layer extends out from all surfaces and edges of the particle. The boundary layer is the distance between the particle surface and the bulk flow. Boundary layers can be defined in terms of the momentum transfer, heat transfer, and mass transfer. Figure 2.5 displays the mass transfer boundary layer between the particle surface and the bulk flow. Within the boundary layer the mass concentration goes from the concentration at the surface of the particle C_s to the concentration in the bulk flow $C_{bulk} = 0$. In this set-up, we assume that the bulk flow acts as a perfect sink, meaning that there is no mass outside of the particle boundary layer.

The shape of the concentration profile for figure 2.5 should be noted as well. The concentration profile is non-linear because turbulent diffusion is not uniform in space. If we

had uniform turbulent diffusion, then there would be a linear concentration profile depicted. Deriving the solution to the diffusion equation (equation 2.29, where u_i, S, and $R = 0$) will give the shape of the concentration profile in figure 2.5.

The first assumption in this system is that inside the boundary layer (BL) $Pe \ll 1$, meaning that diffusion dominates transport within the boundary layer and that the BL is diffusion limited. Outside of the BL, the assumption is that $Pe \gg 1$ so advection dominates and the mass is moved away from the particle as soon as it is outside of the BL. One of the other important assumptions made here is that mass leaves normal to the particle surface only. Using these two assumptions, we create a model for the mass flux based on particle shape and size in chapter 5.

References

Kolmogorov, A. (1941). "The Local Structure of Turbulence in Incompressible Viscous Fluid for Very Large Reynolds' Numbers". In: *Akademiia Nauk SSSR Doklady* 30, pp. 301–305. ISSN: 0002-3264.

Pope, Stephen B. (2000). *Turbulent Flows*. Cambridge: Cambridge University Press. ISBN: 978-0-521-59886-6. DOI: 10.1017/CBO9780511840531.

Chapter 3

Flat Particles

3.1 Introduction

Many natural and industrial processes involve anisotropic particles Voth and Soldati 2017. Until recently, not much research was done on these shapes due to computational and experimental limits. Even with the advances in technology, much of the work has been focused on particles smaller than the Kolmogrov scale, the smallest lengthscale of turbulence Porta et al. 2001; Chevillard and Meneveau 2013; Pujara and E. A. Variano 2017; Zhao, Niranjan R. Challabotla, et al. 2019; Fries et al. 2018. When particles larger than the Kolmogorov scale are investigated, many studies concentrate on fibers Oehmke et al. 2021; Bordoloi, E. Variano, and Gautier Verhille 2020; Bounoua, Bouchet, and G. Verhille 2018; Brouzet, G. Verhille, and Le Gal 2014; Parsa and Voth 2014 or solid 3D shapes Xu and Bodenschatz 2008; Cisse, Homann, and Bec 2013; Byron et al. 2015; Bordoloi and E. Variano 2017; Pujara, Oehmke, et al. 2018. Few studies representing inertial discs Marcus et al. 2014 have been conducted.

A scaling argument analysis by Parsa and Voth (2014) determined the length-scale of relevance for the forcing on fibers larger than the Kolmogorov scale. By assuming that fibers are rotated by an eddy-size on the same scale as the fiber, they derived a -4/3 power-law scaling for inertial fibers. This scaling signals that if the non-dimensional length raised to the -4/3 provides a linear fit, then the particle motion is governed by eddies on the same size-scale as the particle. Bounoua, Bouchet, and G. Verhille (2018) validated this scaling experimentally for the tumbling rate of rigid fibers within the inertial sub-range.

For the larger, three-dimensional inertial particles Bordoloi and E. Variano (2017) and Pujara, Oehmke, et al. (2018) show that with agarose particles of various shapes the tumbling rates and overall enstrophy of a particle follows the same -4/3 scaling law as was derived for fibers. Of the studies on inertial cuboids, few break the motion of the particles into their tumbling (rotation of the symmetry axis) and spinning (rotation around the symmetry axis) components Byron et al. 2015; Bordoloi and E. Variano 2017 to determine the influence of shape on whether or not particles preferentially tumble vs spin.

Table 3.1: Size and shape range for the various particles. δ stands for the thickness of the particles, and R is the radius of the circumcircle.

Shape	Small $\delta = 0.5 \ mm$ $r = 2.5 \ mm$	Medium $\delta = 1 \ mm$ $r = 5 \ mm$	Large $\delta = 2 \ mm$ $r = 10mm$
Triangle	✓	✓	✓
Square		✓	
Hexagon		✓	

Preferential tumbling and spinning for small rods and discs, however, has been well characterized Parsa, Calzavarini, et al. 2012; Chevillard and Meneveau 2013; Gustavsson, Einarsson, and Mehlig 2014; Voth 2015; Pujara and E. A. Variano 2017. In homogeneous, isotropic turbulence (HIT) rods tend to spin more and discs tend to tumble Zhao, Niranjan Reddy Challabotla, et al. 2015; Chevillard and Meneveau 2013; Byron et al. 2015. While close to the wall, both rods and discs show a preferential orientation, in HIT, their orientations are closer to random Parsa, Calzavarini, et al. 2012; Niranjan Reddy Challabotla, Zhao, and Andersson 2015; Zhao, Niranjan Reddy Challabotla, et al. 2015.

In this study, we experimentally evaluate the rotation of flat, disc-like particles in three different shapes and three different sizes, all of which are larger than the Kolmogorov scale. The rotation of the flat particles is broken into its tumbling and spinning components and tested against the -4/3 scaling to see if flat particles follow the same behavior as fibers and cuboids. To our knowledge, this is the first experimental study of flat, anistropic, intertial particles in high Reynolds number flows.

3.2 Laboratory Set-Up

Particles

Experiments were performed on five different flat particles (figure 3.2b). Triangular particles of three different sizes and one size each of square and hexagonal particles were tested in a laboratory setting. The particles were made using polystyrene boards of various thicknesses and a laser cutter. The shapes were inscribed within bounding circles of varying diameters and the thickness was scaled proportionally all of the particles maintain the same aspect ratio. Table 3.1 shows all of the sizes. After the particles were cut with the laser cutter, they were sanded by hand to remove burrs created by melted material sticking to the edges.

Table 3.2: Turbulence and camera parameters for the laboratory experiments. Turbulence parameters taken from Particle Image Velocimetry without large flat particles in the tank.

Motor Frequency f [Hz]	Acquisition Rate [fps]	Integral Length L_I [cm]	Taylor Length λ [mm]	Reynolds Number Re_λ [–]	Kolmogorov Length η [μm]	Kolmogorov Time τ_η [ms]
5-15	700-3000	4.9-7.0	1.7-2.5	303-626	34-72	1.2-5.2

Stirred Tank

The particles were subjected to homogeneous isotropic turbulence within a tank of 60cm cubed (see figure 3.1). The tank was constructed out of a welded stainless steel body with six acrylic panels, one covering each side. Each panel was bolted to the metal frame and a rubber gasket was placed between the panel and the frame to prevent leaking. The tank was filled with tap water and then sealed with a top panel. To remove the bubbles from inside the tank, a small reservoir was attached to the top of the tank, open to the atmosphere. To help with the degassing process, the water in the tank was heated to around 50°C; as the bubbles rose to the top of the tank, the impellers pushed them towards the reservoir where they left the tank and escape to the atmosphere. After the bubbles were removed, the tank cooled for 24 hours before experiments started.

There are eight impellers in the tank: one on each corner of the cube. These impellers are connected to 1.5 kW brushless motors that rotate at frequency (f) to create turbulence inside the tank. The impellers are made of a 17cm diameter disc with eight 5mm blades oriented radially on the disc surface. The rotation rate was the same for all impellers (5Hz, 10Hz or 15Hz), but the direction of rotation was opposite to that of its nearest neighbor (Figure 3.1c).

The turbulence in the tank was characterized using classical two-dimensional particle image velocimetry (2D PIV). The energy dissipation rate and other turbulent quantities are included in table 3.2. Measurements validating these characteristics agree very well with numerical measurements Shin and Koch 2005. The results presented here are taken from Bounoua, Bouchet, and G. Verhille (2018). All of the particles tested lie between the Taylor and Integral lengthscales.

3.3   Methods

Data Collection

Measurements were taken with three Phantom VEO 710L series cameras placed approximately 30 centimeters away from the tank. The cameras were fitted with 50mm zeiss lenses,
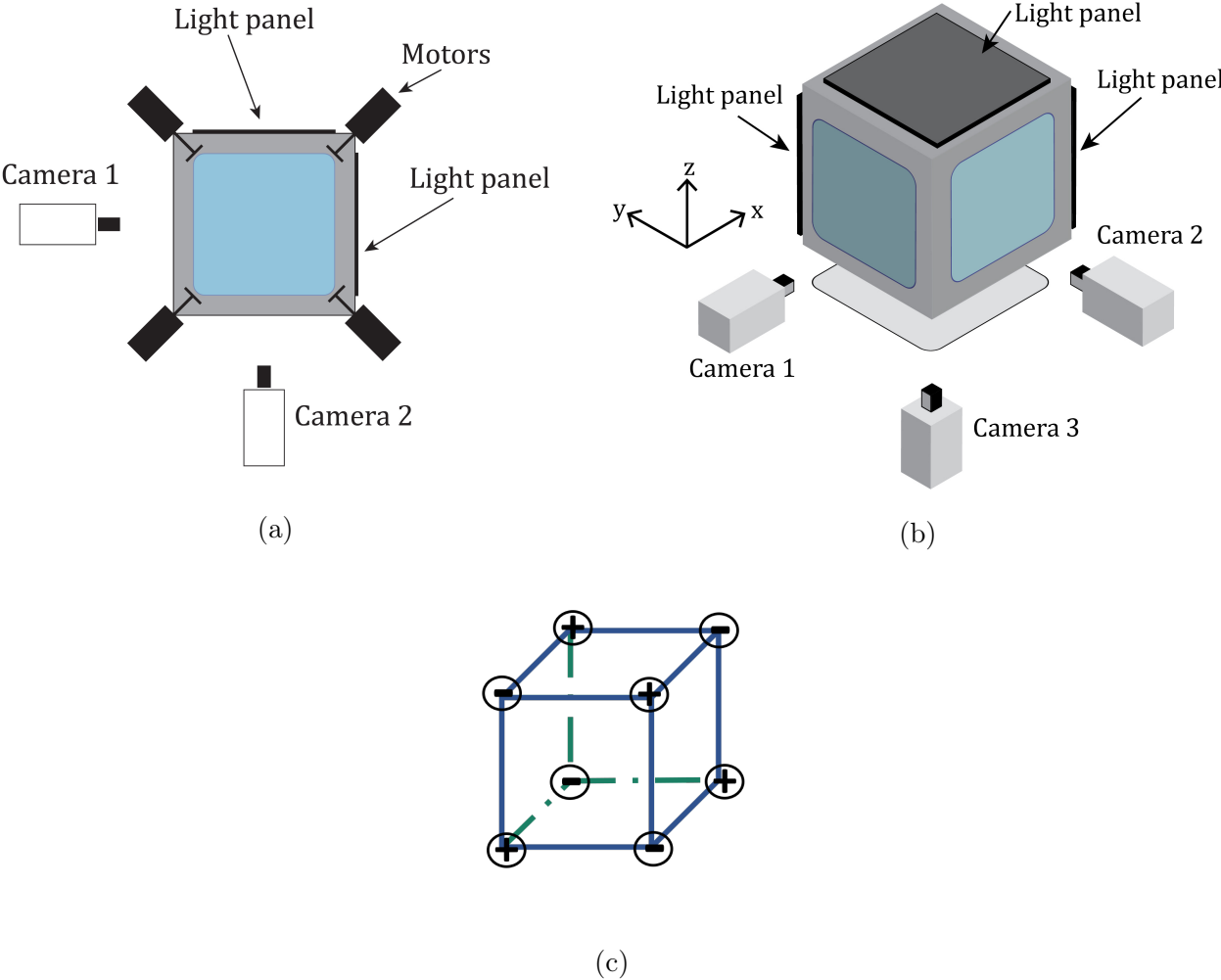
(a)

(b)

(c)

Figure 3.1: Two different views of the turbulence tank. There are motors on all eight corners of the tank. The 3D schematic does not show the motors for clarity. Each camera is opposite a light panel, resulting in backlit photos that are easier to use for path reconstruction.

and recorded images with a 960x800 resolution at 700 - 3000 frames per second (fps) depending on impeller speed. The particles in the tank were backlit by LED panels placed opposite each of the three cameras. Two of the cameras were placed on the sides of the tank, perpendicular to the acrylic panels. The third camera was placed beneath the tank with an additional acrylic shield constructed to divert water in case of leaking from the tank. A schematic of the experimental set-up (Figure 3.1b) shows the placement of the light panels, the cameras, and the motor-impeller combination. The placement of the cameras coincides with the x-, y-, and z- axes of the tank.

20-30 measurements having approximately 10,000 image triplets each were taken for each particle type. The number of measurements depended on the number of particles placed in the tank (between 100 and 150 particles) to make sure sufficient numbers of particle trajectories were captured for statistical convergence. The test for statistical convergence was based on the variance of the particle x vector within a trajectory. The variance of the particle x vector for one trajectory was computed from all of the p_x values in that single trajectory. To determine the number n of trajectories needed for the mean variance $\langle \sigma^2 \rangle$ to converge, the variance across all trajectory $1 - n$ variance values was computed until the addition of an additional trajectory changed the mean variance value by less than 0.005. The variance of the variance method was used as a check because mean values converge faster than variances. If the variance converges within n trajectories, then the mean values will also converge within n trajectories.

The variances converged around 500 trajectories when we set our minimum trajectory length at 100 frames. The 100 frame threshold balances having a sufficiently large number of total trajectory tracks and taking accurate derivatives of the trajectories such that tumbling and spinning can be calculated. For all of the shapes we had at least twice the number of trajectories needed for convergence of the variance. We were able to calculate the location and orientation of the particles within ∼5 pixels or ∼ 0.5mm.

Reconstruction

3D reconstruction of the particle trajectories and orientatons was computed in Matlab. Images collected using the three cameras were binarized, then particles were identified in each image individually using the regionprops function. Each output set corresponded to the edges and centroid of a particle in one image. By only keeping the locations of the edges of the particles, we were able to reduce the size of the data we needed to save, thus allowing for faster computations.

The different perspectives from the three cameras were taken into account after all of the particles had been identified. Once particle edges were identified in the binarized images, the edge coordinates were put into homogeneous coordinates which is a classical way of preparing coordinates that can be projected into 3D space Hartley and Zisserman 2004. Since these coordinates have been located from the flat images, there is some mismatch compared to their true location. The location of the coordinates on the 2D plane was corrected using the parameters gathered during the calibration of the experiments.

The corrected points that composed the edges of the particles were then projected from one image onto another using epipolar lines. Epipolar lines and epipoles are a way to relate the center of one camera to the center of another when the cameras are modeled as pinhole cameras Hartley and Zisserman 2004. Using this relationship, the particles located on one image are then projected onto the other two images. The distance between the projected location from the first image and the identified location within the second image is calculated. When this distance is below some threshold, the particle is kept. This process is repeated for all image pairs and projections are computed in both directions for those image pairs. Thus, one particle has six projections: 3 pairs of planes, each considered in both directions. Only the particles whose projected distances are beneath the threshold for all of the image pairs were kept for 3D reconstruction.

To reconstruct the particles that were identified in all of the images, the particle edge locations and center of mass were projected into 3D space using the projection matrix obtained from the camera calibrations. This gave the 3D points of each reconstructed particle at a single time frame. 3D locations were back-projected from 3D space onto the individual image planes. If the location of the back-projected 3D particle was within some threshold of the particle boundary on the original image plane, then the particle's 3D location was optimized by minimizing the distance between the particle boundary and the back-projected particle location for each of the three images in a given timestep.

Individual 3D-reconstructed particles were linked to trajectories using the nearest-neighbor method described in Ouellette, Xu, and Bodenschatz (2006). For a given particle trajectory S, the location of the particle at time t was compared to the locations of all particles identified at $t + 1$ within a certain distance threshold. The particle location at $t + 1$ that was closest to the particle location of $S(t)$ was added to the trajectory, extending the trajectory to $t+1$. When a conflict arose (multiple particles at $t+1$ with the same distance from $S(t)$), the particle whose orientation at time $t + 1$ was closest to the orientation of $S(t)$ was added to the end of the trajectory. If two locations and two orientations were very similar at $t + 1$, the trajectory was cut.

Once a particle position was added to a trajectory, the particle was removed from the list of identified objects. The trajectory continues to grow in the manner described above until several frames pass where no suitable identified location was detected to add to the trajectory or the trajectory had to be cut due to overlapping. Trajectories were built this way one frame at a time and every particle identified in a given frame was either added to a previous trajectory or was used to start a new trajectory before moving on to the next frame.

(a)

(b)

(c)
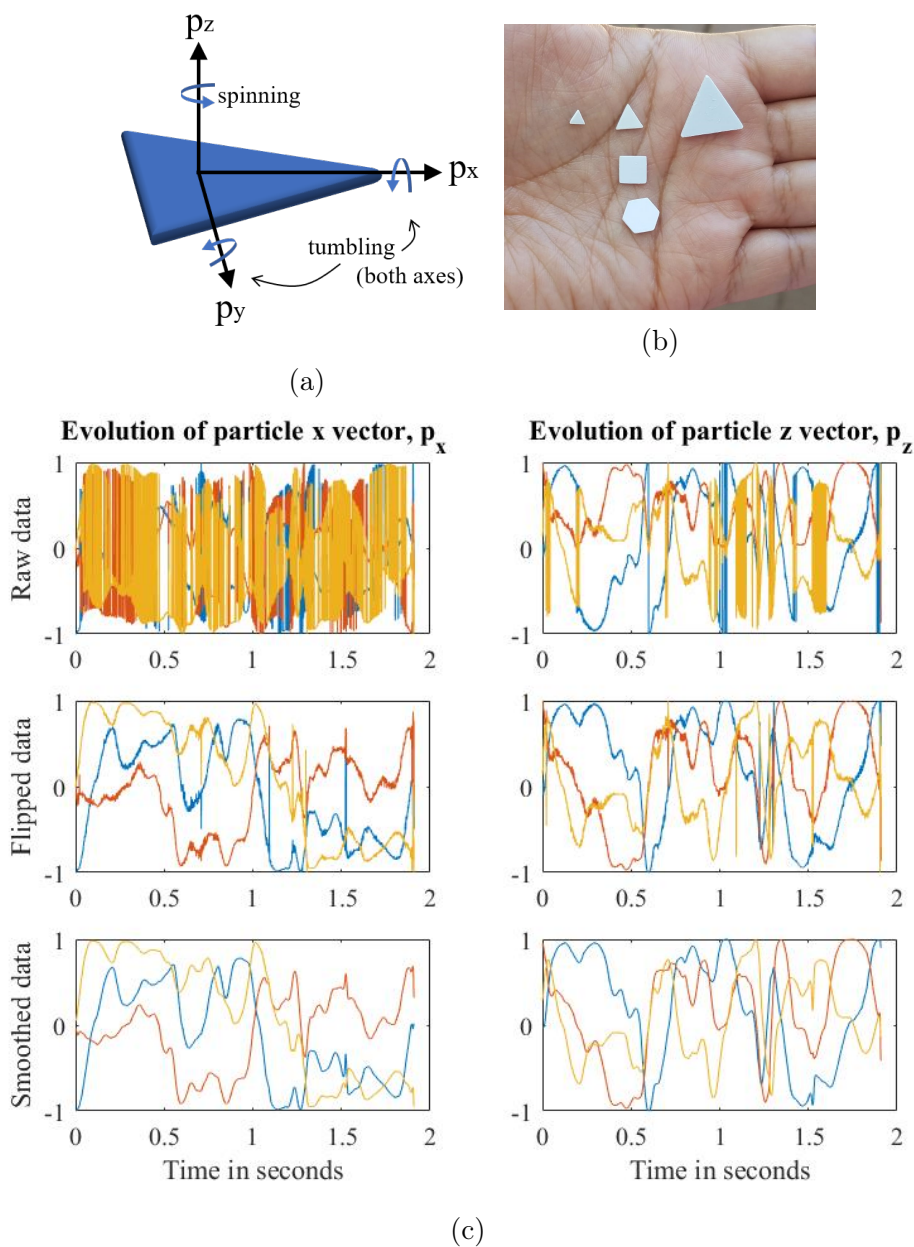
Figure 3.2: (a) An example equilateral triangle particle defines tumbling and spinning axes. (b) Image of the particles tested. (c) The evolution of the p_x and p_z vectors for a sample trajectory. The top panel shows raw trajectory, the middle panel shows flipped trajectory, and the bottom panel shows smoothed trajectory. The three colors correspond to the different components of the particle vectors: x-component is blue, y-component is red, z-component is yellow. The vertical axes for the first and second columns is alignment with the $\hat{x}$ and $\hat{z}$ axes of the tank, respectively.

3.4 Analysis

Post-processing

Evolution of the raw trajectory of a particle can be seen in the top panel of figure 3.2c. This top panel shows the evolution of the particle x vector p_x and the evolution of the particle z vector p_z throughout a single trajectory in the left and right panels, respectively. The p_x vector has more noise than the p_z vector because p_x could possibly be aligned with any of the vertices. We take care of these discrepancies through the "flipping" and optimization processes.

Each particle orientation is computed in its individual frame, so when the particles are linked together in trajectories, sometimes the orientation switches back and forth between which side is "up" and which side is "down". To overcome this, the dot product of $p_z(t+1)$ and $p_z(t)$ was computed. If the result of this dot product was negative, then $p_z(t+1)$ was multiplied by -1 to change its "up" and "down." p_x had a similar "flipping" problem due to a mismatch of which vertex of the particle is aligned with p_x. We aimed to maximize the dot product between $p_x(t+1)$ and $p_x(t)$. Each of the particle vertices in time $t+1$ were compared with $p_x(t)$ and the vertex that was the closest to the previous $p_x(t)$ was taken to be $p_x(t+1)$ and the p_x vector was rotated by factors of $2\pi/n$, where n is number of vertices, to make these align.

To make sure the particle does not flip back and forth too often, $p_z(t)$ and $p_x(t)$ are computed from a trajectory where the previous 50 points have been smoothed. This smoothing is only used to determine whether or not an orientation at a given timestep should be flipped. It is not used outside of this calculation.

The bottom panel of figure 3.2c shows the filtered p_z and p_x vectors. To optimize these vectors, the difference between the filtered vectors and the flipped vectors was minimized. The filtered vectors were computed just for this optimization process. 7 points were used to apply a filter to both p_z and p_x giving $p_{z,f}$ and $p_{x,f}$. Determining the number of filter points n to use was done by plotting the mean tumbling rate squared $\langle \Omega_t \Omega_t \rangle$ against the number of filter points used to compute $\langle \Omega_t \Omega_t \rangle$ against n and selecting the lowest n in the plateau region.

Computation of Rotation

The change in particle location and orientation can be computed by determining the particle's translation vector T and rotation matrix $\boldsymbol{R}$ compared to some reference position. The reference particle center of mass is located at the center of the tank, with p_z pointing upward along the tank's z-axis and p_x (aligned with particle vertex) and p_y lying flat along the tank's x- and y-axes.

The rotation matrix $\boldsymbol{R} = \boldsymbol{R}_t \boldsymbol{R}_s$ is solved for from matching the reference triangle to the outline in the images. $\boldsymbol{R}_t$ and $\boldsymbol{R}_s$ are then calculated from the particle orientation vectors, which are known due to their relationship with $\boldsymbol{R}$.

$$p_x = \boldsymbol{R} \begin{bmatrix} 1 \\ 0 \\ 0 \end{bmatrix}, \quad p_y = \boldsymbol{R} \begin{bmatrix} 0 \\ 1 \\ 0 \end{bmatrix}, \quad p_z = \boldsymbol{R} \begin{bmatrix} 0 \\ 0 \\ 1 \end{bmatrix} \tag{3.1}$$

To find $\boldsymbol{R}_t$ knowledge about spinning is used. $p_z = \boldsymbol{R} \begin{bmatrix} 0 \\ 0 \\ 1 \end{bmatrix}$ as stated above, but $\boldsymbol{R}_s \begin{bmatrix} 1 \\ 0 \\ 0 \end{bmatrix} = \begin{bmatrix} 1 \\ 0 \\ 0 \end{bmatrix}$ since spinning is always around the z-axis of the particles. Therefore p_x is actually $p_x = \boldsymbol{R}_t \begin{bmatrix} 1 \\ 0 \\ 0 \end{bmatrix}$ which gives us $\boldsymbol{R}_t$ and from there we can find $\boldsymbol{R}_s$.

The tumbling rate vector Ω_t is calculated directly from p_z. Since tumbling is the evolution of p_z, Ω_t is computed by calculating the numerical gradient of the p_z vector.

Calculating the spinning rate vector is a bit more complicated compared to tumbling. p_x is the $\hat{x}$ vector of the tank rotated into the particle frame of reference such that $p_x = \boldsymbol{R} \begin{bmatrix} 1 \\ 0 \\ 0 \end{bmatrix}$. Ultimately the spinning vector $e_s = \boldsymbol{R}_s \begin{bmatrix} 1 \\ 0 \\ 0 \end{bmatrix}$ is used to determine the spinning evolution, but it is challenging to compute $\boldsymbol{R}_s$ directly. Instead, p_x is used to compute $\boldsymbol{R}_s$ where $e_s = \boldsymbol{R}_t^{-1} p_x = \boldsymbol{R}_t^{-1} \boldsymbol{R} \begin{bmatrix} 1 \\ 0 \\ 0 \end{bmatrix} = \boldsymbol{R}_t^{-1} \boldsymbol{R}_t \boldsymbol{R}_s \begin{bmatrix} 1 \\ 0 \\ 0 \end{bmatrix} = \boldsymbol{R}_s \begin{bmatrix} 1 \\ 0 \\ 0 \end{bmatrix}$.

After computing e_s, the evolution of the spinning vector is used to find Ω_s. The spinning rate is given by

$$\dot{e}_s = \Omega_s \times e_s \tag{3.2}$$

$$\dot{e}_s = -e_s \times \Omega_s \tag{3.3}$$

To take the inverse of e_s the cross product matrix is used which gives $\boldsymbol{C_e}$ or the matrix resulting from crossing e_s with $\hat{z}$. Then the inverse of $\boldsymbol{C_e}$ times $\dot{e}_s$ can be solved for Ω_s.

Example trajectories of Ω_t and Ω_s are in figure 3.3. In figure 3.3a, all three components of rotation are shown. The z-component represents the spinning of the particle, and is much smaller compared to the other two components which represent the tumbling. These components were computed from the particle orientation vectors, and were used as the intermediate step between figures 3.2 and 3.4.

As of August 2021, the analysis and post-processing code are still being checked for quality control.

3.5 Results and Discussion

Each tumbling and spinning rate was considered individually and the variance was computed across all tumbling and spinning value for each shape-size-frequency combination (see figure 3.4 and 3.3). Following the definitions in Pujara and E. A. Variano 2017, the variance of the tumbling was taken to be the sum of the variance around the particle x-axis and the particle y-axis. The variances were normalized by the Kolmogorov time squared and were plotted as
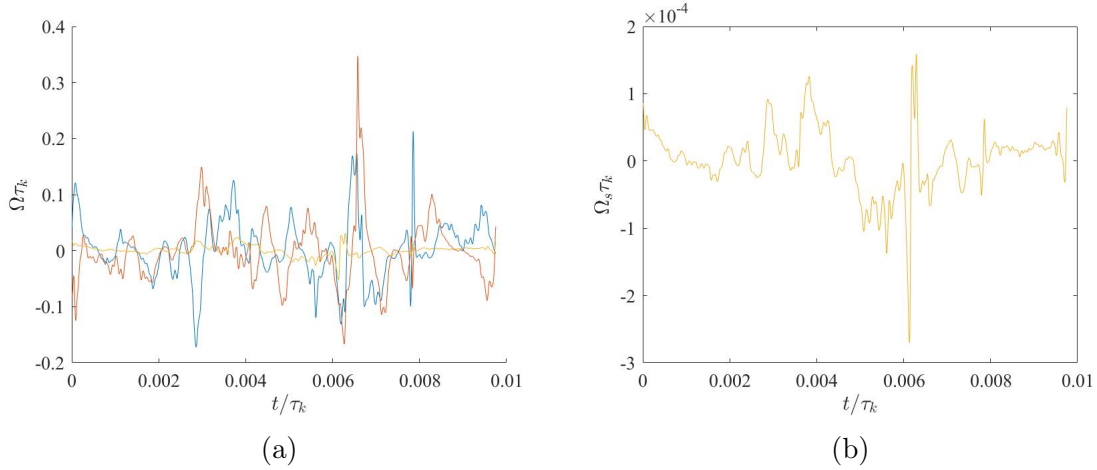
Figure 3.3: Evolution of tumbling and spinning in time. The three colors correspond to the different components of the particle rotation: x-component is blue, y-component is red, z-component is yellow. (a) Shows the total particle rotation including tumbling (blue and red) and spinning (yellow). The yellow component (spinning) is much smaller than the other two (which contribute to tumbling) and thus is also shown in expanded axes in figure (b).

a function of the radius (of the circle the shapes were inscribed within) normalized by the Kolmogorov length-scale.

Figure 3.4a shows two important results: 1) the variance of the tumbling rate collapses on a $-4/3$ power law scaling, suggesting that particle rotation is dictated by fluid motions at the same size-scale of the circle inscribing the particles; and 2) for these flat particles, shape does not have a large influence on their overall motion. These two statements show a very important characteristic of the inertial subrange. The agreement of flat particles with the $-4/3$ scaling emphasizes the result that within the inertial subrange, particle motion is dictated by eddies of the same scale as the particle, regardless of particle shape or dimensionality Parsa and Voth 2014. The difference between fibers (1D), flat particles (2D), and cuboids (3D) is in determining which scale of the particle is the characteristic length-scale that corresponds to the forcing eddy size. This characteristic lengthscale could be the particle length, the particle diameter, the sphere equivalent diameter of the particle, etc.

Fries et al. (2018) did experiments with micron-sized triangular particles, and found that the triangular particles followed the Jeffrey orbits derived for spheroids, suggesting that even though the shape is not a disc, the motion is the same as for discs. The shape independence in figure 3.4a suggests the same for large particles.

We can compare inertial-subrange trends with dissipation-range limits as seen in figure 3.4a. The purple cross on the vertical axis represents the rotational variance of small, inertia-less oblate spheroids, or disc-like particles, in homogeneous, isotropic turbulence Pujara and E. A. Variano 2017. This value was computed as the particles followed tracer path-lines in direct numerical simulation (DNS). Starting at the purple cross we draw a horizontal
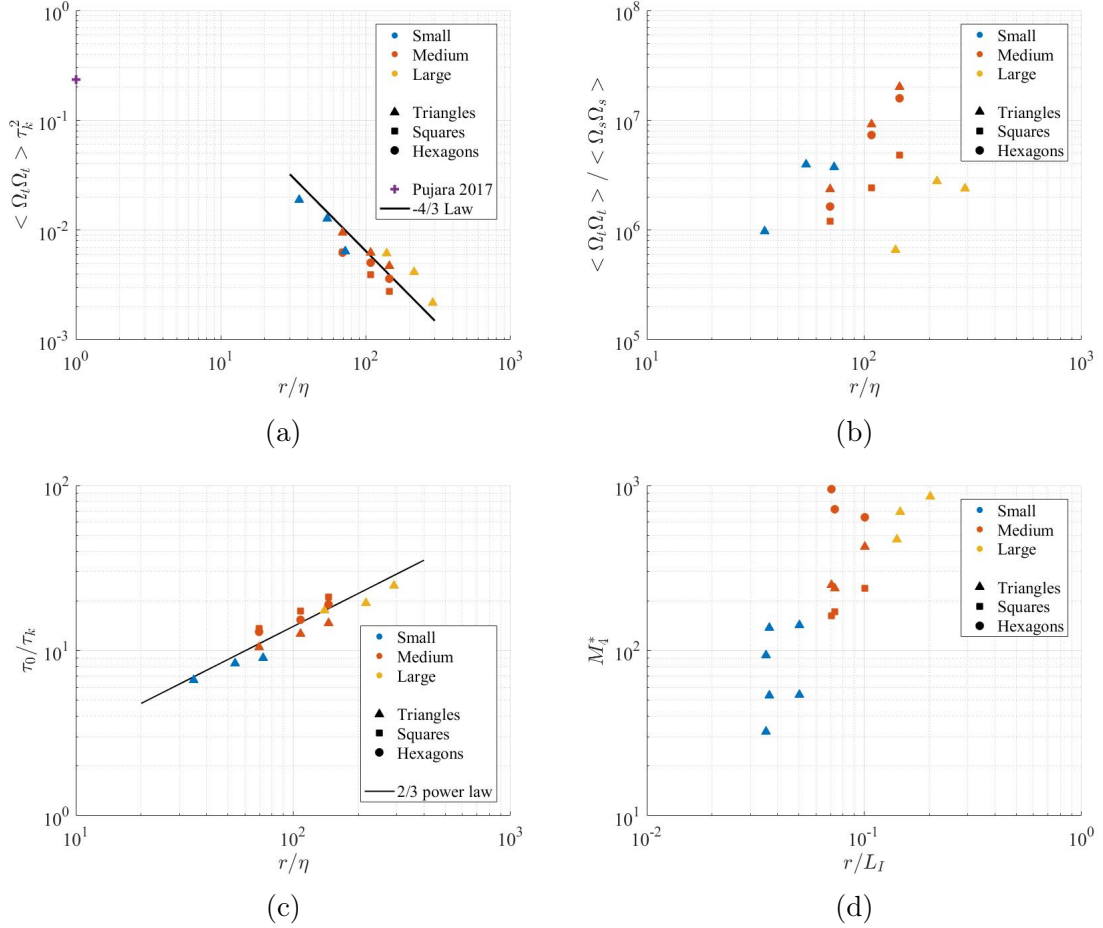
Figure 3.4: (a) Variance of the tumbling rate. (b) Variance of tumbling compared to variance of spinning. (c) Zero-crossing time for tumbling. (d) Kurtosis of the tumbling rate. In all plots, particle size r is the radius of the bounding circle. In (a)-(c) quantities are normalized with Kolmogorov microscales; in (d) quantities are normalized by the integral length.
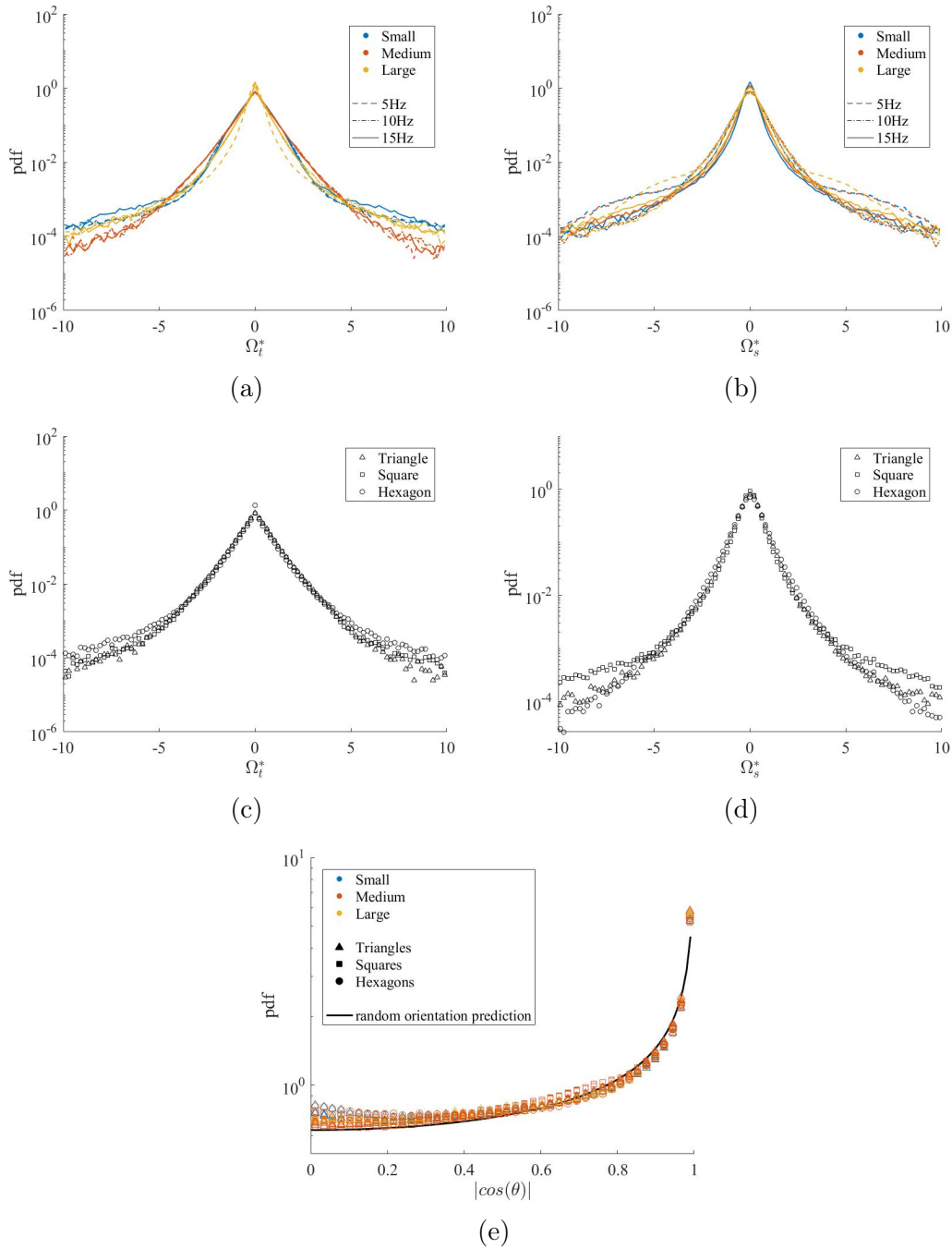
Figure 3.5: Normalized and centered pdfs for tumbling and spinning rates. (a) pdf for the tumbling rate of all triangles (b) pdf for the spinning rate of all triangles (c) pdf for the tumbling rate of the medium shapes at 5Hz. (d) pdf for the spinning rate of the medium shapes at 5Hz. (e) Preferential Orientation of $cos\theta$ where θ is the angle between p_x and Ω_t. This angle is compared to a random orientation (black line).

line across figure 3.4a. By extending the line created by fitting the $-4/3$ power-law to the data, we can determine where this line intersects with the horizontal line from Pujara and E. A. Variano 2017. These two lines intersect at approximately $r = 7\eta$, showing that the Kolmogorov scaling works within our experimental regime since the emipirical limit for this scaling law is approximately 10η Tennekes and Lumley 1972.

The variance of the tumbling rate was much larger than the variance of the spinning rate (figure 3.4b). This is to be expected given the motion of small discs in HIT Zhao, Niranjan Reddy Challabotla, et al. 2015; Chevillard and Meneveau 2013; Byron et al. 2015 and also agrees with what was qualitatively observed while the experiments were being conducted. Additionally, it is in reverse from what was seen by Oehmke et al. 2021 when fibers were examined. This result, 'fibers spin, discs tumble' is the same as that for sub-Kolmogorov-scale particles Byron et al. 2015; Chevillard and Meneveau 2013; Zhao, Niranjan Reddy Challabotla, et al. 2015. The fact that some trajectories were longer than others did not affect the statistical quantities because all trajectories were independent and identically distributed and we confirmed that the data in each track was uncorrelated with its trajectory length.

The zero-crossing time in figure 3.4c shows a $2/3$ power-law fit coming from the scaling in Bordoloi, E. Variano, and Gautier Verhille (2020). Zero-crossing time τ_0 is defined as the time when the Lagrangian correlation function of a quantity goes to zero Shin and Koch 2005. In figure 3.4c the time when the Lagrangian correlation function of the tumbling rate goes to zero is shown. Here, τ_0 scales as u_r/r where u_r is the eddy-turnover time at the size of the particle. $\tau_0 \sim u_r/r \sim r^{2/3}\epsilon^{-1/3}$ signaling that eddies of the same size as the particle strongly contribute to their rotation.

The plots in figures 3.5a-3.5d show the probability density function (pdf) for the tumbling and spinning components of rotation across the shape-frequency space. The pdfs are centered by subtracting the mean and are normalized by the standard deviation. The asterisk denotes the centered and normalized tumbling and spinning quantities. The left-hand-side of the panel (3.5a, 3.5c) shows the pdfs for the tumbling rate and the right-hand side of the panel (3.5b, 3.5d) shows the pdfs of the spinning rate. Across the top (3.5a, 3.5b) the shapes are all triangles at all frequencies and across the bottom (3.5c, 3.5d) the pdfs show all shapes at only 5Hz motor driving frequency. All four of these plots are super-Gaussian showing large tails and a Kurtosis greater than 3. This signifies that the particles tend to drift through the flow for a long time before experiencing extreme events. The tails for tumbling are a bit wider than the tails for spinning (for the triangular particles); tumbling rate pdfs at all three frequencies seem to have a very similar shape except for the large triangles at 5Hz where the pdf is slightly below the other values for $\Omega_t \approx \pm 2$. Similarly, the spinning rate shows a deviation with the pdf of the 5Hz frequency where the tails of three sizes of triangles are larger than the tails of the other two frequencies when $\Omega_s \gtrapprox \pm 3$. Concerning the different-shaped particles, we see very little difference in the pdf based on shape alone for both tumbling and spinning rates.

We tested to see if there was any preferential orientation regarding which axis the particles rotated around. That is, we looked at the angle between the particle x vector and the Ω_t

Table 3.3: The moments of the particle rotation results. Variance* is normalized by the Kolmogorov time squared.

(a) Tumbling

	Frequency [Hz]	Mean [sec^{-1}]	Variance [sec^{-2}]	Variance* [–]	Kurtosis [–]
Small Triangle	5	-0.269	702	0.019	143
	10	-0.509	2768	0.013	138
	15	-0.613	4518	0.006	93
Medium Triangle	5	-0.314	358	0.009	424
	10	-0.694	1369	0.006	238
	15	-0.945	3354	0.005	251
Large Triangle	5	-0.126	230	0.006	859
	10	-0.348	909	0.004	690
	15	-0.438	1553	0.002	470
Square	5	-0.230	236	0.006	238
	10	-0.381	854	0.004	172
	15	-0.550	1950	0.003	163
Hexagon	5	-0.180	234	0.006	642
	10	-0.507	1097	0.005	720
	15	-1.40	2544	0.004	948

(b) Spinning

	Frequency [Hz]	Mean$\times 10^{-5}$ [sec^{-1}]	Variance$\times 10^{-4}$ [sec^{-2}]	Variance*$\times 10^{-9}$ [–]	Kurtosis [–]
Small Triangle	5	6.378	7.165	19.08	54
	10	-4.547	6.988	3.194	54
	15	13.57	12.00	1.697	32
Medium Triangle	5	-0.971	1.520	4.047	226
	10	-9.712	1.484	0.679	200
	15	5.312	1.666	0.345	200
Large Triangle	5	7.663	3.469	9.239	426
	10	-9.336	3.241	1.482	357
	15	10.13	6.518	0.917	194
Square	5	-4.242	1.960	5.218	250
	10	-1.508	3.543	1.619	118
	15	-2.713	4.060	0.571	91
Hexagon	5	5.492	1.438	3.829	310
	10	-0.903	1.493	0.682	428
	15	-0.421	1.606	0.226	405

vector to determine if the particles rotated preferentially around an a certain edge or vertex. Taking the dot product of p_x and Ω_t gives the cosine of the angle between the two vectors. In figure 3.5e the absolute value of this dot product is plotted in the individual symbols. This is compared to the random orientation of a particle which is predicted by Brouzet, G. Verhille, and Le Gal 2014. The experimental data fits well with the random-orientation prediction, suggesting that the flat particles do not have a preferential orientation in HIT. This agrees with the literature about small inertial discs in HIT Parsa, Calzavarini, et al. 2012; Niranjan Reddy Challabotla, Zhao, and Andersson 2015; Zhao, Niranjan Reddy Challabotla, et al. 2015.

While many of our results are similar to what can be expected of small discs, the evolution of the flatness of the pdfs (see table 3.3) is not yet well explained. There is not a clear trend for the kurtosis of the pdfs (figure 3.4d) and kurtosis values for the tumbling and spinning pdfs are almost an order of magnitude larger than those of fibers Oehmke et al. 2021. This suggests that the flat particles' experience of extreme events is higher than for inertial fibers.

3.6 Conclusion

In this chapter the rotation and orientation of flat particles in homogeneous, isotropic turbulence was studied experimentally. These particles showed no preferential orientation with the tumbling or spinning functionality along the particle surface or edges. The variance of the tumbling was larger than the variance of the spinning, and both followed a $-4/3$ power-law scaling. The scaling was similar to that of fibers and cuboids suggesting that the particle motion is dictated by fluid structures on the same size scale as the particles, regardless of shape. While all particle shapes follow the $-4/3$ scaling, the characteristic length changed based on particle shape. For flat particles, the variance of the tumbling collapsed with respect to the diameter of the circle the particle was inscribed within. Overall these results are similar to what has been seen for inertial disc-like particles whose sizes are smaller than the Kolmogorov length.

Acknowledgement

References

Bordoloi, Ankur D. and Evan Variano (2017). "Rotational kinematics of large cylindrical particles in turbulence". en. In: *Journal of Fluid Mechanics* 815, pp. 199–222. ISSN: 0022-1120, 1469-7645. DOI: `10.1017/jfm.2017.38`.

Bordoloi, Ankur D., Evan Variano, and Gautier Verhille (2020). "Lagrangian Time Scale of Passive Rotation for Mesoscale Particles in Turbulence". English. In: *Frontiers in Marine Science* 7. ISSN: 2296-7745. DOI: `10.3389/fmars.2020.00473`.

Bounoua, S., G. Bouchet, and G. Verhille (2018). "Tumbling of Inertial Fibers in Turbulence". In: *Physical Review Letters* 121.12, p. 124502. DOI: `10.1103/PhysRevLett.121.124502`.

Brouzet, C., G. Verhille, and P. Le Gal (2014). "Flexible Fiber in a Turbulent Flow: A Macroscopic Polymer". In: *Physical Review Letters* 112.7, p. 074501. DOI: `10.1103/PhysRevLett.112.074501`.

Byron, M., J. Einarsson, K. Gustavsson, G. Voth, B. Mehlig, and E. Variano (2015). "Shape-dependence of particle rotation in isotropic turbulence". en. In: *Physics of Fluids* 27.3, p. 035101. ISSN: 1070-6631, 1089-7666. DOI: `10.1063/1.4913501`.

Challabotla, Niranjan Reddy, Lihao Zhao, and Helge I. Andersson (2015). "Orientation and rotation of inertial disk particles in wall turbulence". English. In: *Journal of Fluid Mechanics* 766. ISSN: 00221120. DOI: `http://dx.doi.org/10.1017/jfm.2015.38`.

Chevillard, Laurent and Charles Meneveau (2013). "Orientation dynamics of small, triaxial–ellipsoidal particles in isotropic turbulence". en. In: *Journal of Fluid Mechanics* 737, pp. 571–596. ISSN: 0022-1120, 1469-7645. DOI: `10.1017/jfm.2013.580`.

Cisse, Mamadou, Holger Homann, and Jeremie Bec (2013). "Slipping motion of large neutrally-buoyant particles in turbulence". In: *Journal of Fluid Mechanics* 735. ISSN: 0022-1120, 1469-7645. DOI: `10.1017/jfm.2013.490`.

Fries, J., M. Vijay Kumar, B. Mekonnen Mihiretie, D. Hanstorp, and B. Mehlig (2018). "Spinning and tumbling of micron-sized triangles in a micro-channel shear flow". In: *Physics of Fluids* 30.3, p. 033304. ISSN: 1070-6631. DOI: `10.1063/1.5020383`.

Gustavsson, K., J. Einarsson, and B. Mehlig (2014). "Tumbling of Small Axisymmetric Particles in Random and Turbulent Flows". en. In: *Physical Review Letters* 112.1, p. 014501. ISSN: 0031-9007, 1079-7114. DOI: `10.1103/PhysRevLett.112.014501`.

Hartley, Richard and Andrew Zisserman (2004). *Multiple View Geometry in Computer Vision*. 2nd ed. Cambridge: Cambridge University Press. ISBN: 978-0-521-54051-3. DOI: `10.1017/CBO9780511811685`.

Marcus, Guy G, Shima Parsa, Stefan Kramel, Rui Ni, and Greg A Voth (2014). "Measurements of the solid-body rotation of anisotropic particles in 3D turbulence". en. In: *New Journal of Physics* 16.10, p. 102001. ISSN: 1367-2630. DOI: `10.1088/1367-2630/16/10/102001`.

Oehmke, Theresa B., Ankur D. Bordoloi, Evan Variano, and Gautier Verhille (2021). "Spinning and tumbling of long fibers in isotropic turbulence". In: *Physical Review Fluids* 6.4, p. 044610. DOI: `10.1103/PhysRevFluids.6.044610`.

Ouellette, Nicholas T., Haitao Xu, and Eberhard Bodenschatz (2006). "A quantitative study of three-dimensional Lagrangian particle tracking algorithms". en. In: *Experiments in Fluids* 40.2, pp. 301–313. ISSN: 1432-1114. DOI: 10.1007/s00348-005-0068-7.

Parsa, Shima, Enrico Calzavarini, Federico Toschi, and Greg A. Voth (2012). "Rotation Rate of Rods in Turbulent Fluid Flow". In: *Physical Review Letters* 109.13, p. 134501. DOI: 10.1103/PhysRevLett.109.134501.

Parsa, Shima and Greg A. Voth (2014). "Inertial Range Scaling in Rotations of Long Rods in Turbulence". In: *Physical Review Letters* 112.2, p. 024501. DOI: 10.1103/PhysRevLett.112.024501.

Porta, A. La, Greg A. Voth, Alice M. Crawford, Jim Alexander, and Eberhard Bodenschatz (2001). "Fluid particle accelerations in fully developed turbulence". en. In: *Nature* 409.6823, pp. 1017–1019. ISSN: 0028-0836. DOI: 10.1038/35059027.

Pujara, Nimish, Theresa B. Oehmke, Ankur D. Bordoloi, and Evan A. Variano (2018). "Rotations of large inertial cubes, cuboids, cones, and cylinders in turbulence". en. In: *Physical Review Fluids* 3.5. ISSN: 2469-990X. DOI: 10.1103/PhysRevFluids.3.054605.

Pujara, Nimish and Evan A. Variano (2017). "Rotations of small, inertialess triaxial ellipsoids in isotropic turbulence". In: *Journal of Fluid Mechanics* 821, pp. 517–538. ISSN: 0022-1120, 1469-7645. DOI: 10.1017/jfm.2017.256.

Shin, Mansoo and Donald L. Koch (2005). "Rotational and translational dispersion of fibres in isotropic turbulent flows". en. In: *Journal of Fluid Mechanics* 540, pp. 143–173. ISSN: 1469-7645, 0022-1120. DOI: 10.1017/S0022112005005690.

Tennekes, Henk and John L. Lumley (1972). *A First Course in Turbulence*. en. Cambridge, MA, USA: MIT Press. ISBN: 978-0-262-20019-6.

Voth, Greg A. (2015). "Disks aligned in a turbulent channel". en. In: *Journal of Fluid Mechanics* 772, pp. 1–4. ISSN: 0022-1120, 1469-7645. DOI: 10.1017/jfm.2015.144.

Voth, Greg A. and Alfredo Soldati (2017). "Anisotropic Particles in Turbulence". In: *Annual Review of Fluid Mechanics* 49.1, pp. 249–276. DOI: 10.1146/annurev-fluid-010816-060135.

Xu, Haitao and Eberhard Bodenschatz (2008). "Motion of inertial particles with size larger than Kolmogorov scale in turbulent flows". In: *Physica D: Nonlinear Phenomena*. Euler Equations: 250 Years On 237.14, pp. 2095–2100. ISSN: 0167-2789. DOI: 10.1016/j.physd.2008.04.022.

Zhao, Lihao, Niranjan R. Challabotla, Helge I. Andersson, and Evan A. Variano (2019). "Mapping spheroid rotation modes in turbulent channel flow: effects of shear, turbulence and particle inertia". en. In: *Journal of Fluid Mechanics* 876, pp. 19–54. ISSN: 0022-1120, 1469-7645. DOI: 10.1017/jfm.2019.521.

Zhao, Lihao, Niranjan Reddy Challabotla, Helge I. Andersson, and Evan A. Variano (2015). "Rotation of Nonspherical Particles in Turbulent Channel Flow". In: *Physical Review Letters* 115.24, p. 244501. DOI: 10.1103/PhysRevLett.115.244501.

Chapter 4

Creating Particles

4.1 Introduction

Mass transfer is an important topic in many areas of science and engineering Bird, Stewart, and Lightfoot 2007; Nazaroff and Alvarez-Cohen 2001. Industrial examples include chemical reactors Boon-Long, Laguerie, and Couderc 1978; Sano, Yamaguchi, and Adachi 1974 and pharmaceuticals Grijseels, Crommelin, and Blaey 1981. Environmental examples include biomass decay by bacteria Nazaroff and Alvarez-Cohen 2001; Stocker et al. 2008; Kiørboe et al. 2002, zooplankton finding mates Bagøien and Kiørboe 2005, and ctenophore locomotion Sasson, Jacquez, and Ryan 2018. In this chapter I investigate dissolution rates of freely moving and dissolving non-spherical particles in turbulence. This has the important application of describing solute transport and waste removal away from drifting oceanic organisms such as ctenophores.

Direct measurements of mass transfer rates in environmental applications traditionally used gypsum (plaster of Paris) to measure flow velocity via dissolution rates in both laboratory and field experiments Porter, Sanford, and Suttles 2000; Angradi and Hood 1998; Baird and Atkinson 1997; Pachon-Rodriguez and Colombani 2013. Before going to the field, laboratory calibrations were used to correlate flowrate with dissolution Angradi and Hood 1998; Baird and Atkinson 1997; Pachon-Rodriguez and Colombani 2013; Thompson and Glenn 1994. Plaster of Paris was molded into shapes such as spheres Porter, Sanford, and Suttles 2000, cubes Angradi and Hood 1998, and corals Baird and Atkinson 1997, before being fixed in place as water flowed past. The results of these experiments were reliable only under certain conditions: the flow statistics of the calibration flow system needed to match the flow statistics of the natural environment where the method was deployed. More recent studies used x-Ray Computed Tomography (CT) scanning and Digital Holographic Microscopy to calculate the dissolution rate of gypsum forms Feng et al. 2017; Chang et al. 2013. These methods did not require comparisons between the rate of dissolving in a laboratory flow and that of the field to find a dissolution rate, leading to more flexibility in experimental set-ups. Nonetheless, these objects were still fixed in space.

Several other studies have directly measured mass transfer rates of freely moving objects Huang, Moore, and Ristroph 2015; Sano, Yamaguchi, and Adachi 1974; Machicoane, Bonaventure, and Volk 2013; Levins and Glastonbury 1972; Boon-Long, Laguerie, and Couderc 1978, but in these the density of the dissolving objects was not customizable depending on the needs of the researchers. Granular particles Sano, Yamaguchi, and Adachi 1974 and spheres Sano, Yamaguchi, and Adachi 1974; Machicoane, Bonaventure, and Volk 2013; Levins and Glastonbury 1972; Boon-Long, Laguerie, and Couderc 1978 in turbulence are some of the studies that have been investigated in freely moving suspensions. In the experiments by Sano, Yamaguchi, and Adachi (1974) and Levins and Glastonbury (1972), mass transfer rates of granular particles and spherical ion exchange beads of relatively small sizes (60-600μm in diameter) were characterized using the Schmidt ($Sc = \nu/\mathcal{D}$) and Sherwood ($Sh = kd_p/\mathcal{D}$) numbers Sano, Yamaguchi, and Adachi 1974; Levins and Glastonbury 1972. The Schmidt number describes the ratio of momentum diffusion to mass diffusion with ν being the kinematic viscosity [$(length)^2/(time)$] and $\mathcal{D}$ the mass diffusivity [$(length)^2/(time)$]. The Sherwood number is often written as a function of the Schmidt number, and relates the convective mass transfer rate to the diffusion rate. In the Sherwood number, k is the mass transfer coefficient [$(length)/(time)$] and d_p is the particle diameter; $\mathcal{D}$ is the mass diffusivity, same as in the Schmidt number. Boon-Long, Laguerie, and Couderc (1978) did similar experiments with spherical benzoic acid particles (2.2-4.3mm in diameter) dissolving in water Boon-Long, Laguerie, and Couderc 1978. We are interested in measuring freely moving particles as well, but with larger particles in a variety of anisotropic shapes and whose density we can control.

For experiments with larger particles, Machicoane, Bonaventure, and Volk (2013) used ice balls (1-3cm in diameter) to study the heat transfer rates of melting. The authors placed the ice balls in a turbulent von Kármán apparatus with parallel lighting and used afocal shadowgraphy to measure melting rates of the spheres. In comparing ice balls that were fixed in space with those that could freely move about, the authors found that the shape of the fixed ice sphere became ellipsoidal over its melting period due to the anisotropy of the flow, while the ice sphere that was freely moving melted isotropically in all of the tested flows Machicoane, Bonaventure, and Volk 2013. The authors predict this could be due to the particle's ability to rotate while it is melting Machicoane, Bonaventure, and Volk 2013.

In this chapter, I focus on creating a material that will allow for study of freely-moving neutrally buoyant particles which dissolve along their Lagrangian trajectories. Neither gypsum, ice, nor sugar alone meet the requirement of neutral buoyancy. Therefore I have developed a sugar-glass-sphere compound that can be used to measure dissolution in a similar manner as gypsum. These particles have a more precise neutral buoyancy allowing me to access different turbulent regimes, and even quiescent flows. In this chapter, I explain the method for manufacturing such particles and use example particles to explore how shape affects the mass transfer rate from a particle's surface in a turbulent flow.
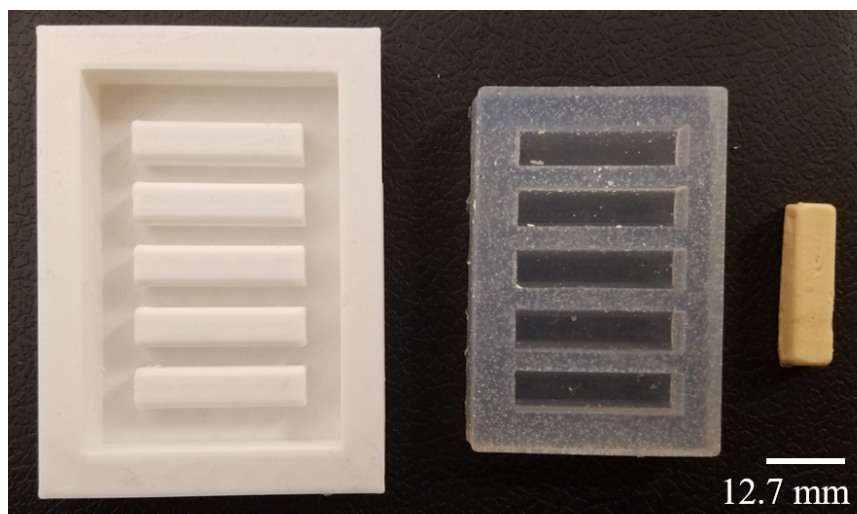
Figure 4.1: 3D-printed positive rod-shaped mold, negative silicone mold, and finished neutrally buoyant rod-shaped particle (from left to right).

4.2   Methods

Fabrication of Particles

Neutrally buoyant sugar-glass particles were made from a mixture of sucrose, dextrose, and hollow glass spheres, which was heated and poured into molds where they cooled and hardened. A series of positive and negative molds was created (shown in figure 4.1). The first mold is a positive mold of the particles, and was made using the Monoprice Mini 3D printer and PLA plastic. The second mold, made out of silicone, is a negative mold of the particles. Vegetable oil was used as a release agent and applied to the positive mold before the mixing of silicone began. The silicone was mixed by combining reagents A and B of PlatSil® 73-15 Liquid Rubber according to the manufacturer's direction, using equal proportions by weight. Mixed silicone was poured into the oiled positive mold and set for 5 hours before it was demolded. Excess rubber around the edges was trimmed with a razor blade.

Once the silicone molds were created, they were filled with the cooked sugar-glass recipe to make the particles. The recipe required mixing 24.0g of sucrose (Fisher Scientific S5-3), 1.5g of dextrose (Fisher Scientific BP350-1), and 5.55g of hollow glass spheres (3M™ Glass Bubbles K37) in a 100mL beaker. Then 10mL of deionized water was added to help combine the ingredients into a slurry. The ingredients were added one-by-one and the cumulative mass of the combined ingredients and the beaker was recorded between consecutive ingredient additions. The stirrer bar and thermometer were added to the beaker and recorded. Recording the mass of each component was essential to having a consistent water concentration in the final particle. The size of the beaker was important for achieving

the proper consistency of the mixture before it was molded. The thermometer gave the most accurate temperature readings when it was submerged in at least one inch of the mixture. Working with this constraint, a 100mL beaker provided the most consistent results regarding temperature measurements and the volume capacity of the beaker to avoid the mixture over-boiling.

The mixture was heated on a hot plate with an average steady-state surface temperature of 256 °C $\pm$ 2 °C. As the mixture cooked, the total mass was monitored to measure the amount of water that had evaporated. The mixture was stirred occasionally to prevent burning on the bottom of the beaker. Minimal stirring helped prevent crystallization of the mixture. When the water concentration reached $\sim$ 5% of the total mass the mixture was poured into the silicone molds. A water concentration of $\sim$ 5% was normally achieved at a temperature of 121 °C $\pm$ 2 °C (about 20 minutes after boiling). At this point, the mixture was light tan in color, and a blob of material, when dropped into cold water, forms a filament which easily snaps. One batch of the above recipe filled approximately two of the silicone molds pictured in figure 4.1.

The cooked slurry solidified quickly after it was removed from the heat, which made casting the particles a time-sensitive process. The beaker was insulated with a neoprene beverage sleeve to help mitigate this problem. The rapid cooling did not leave enough time for any air bubbles introduced when pouring the mixture to rise and escape from the mold before the shape hardened. To minimize the number of trapped bubbles, the mixture was poured into the center of the mold cavity; the mixture flowed out from the center to fill the corners. This technique slightly reduced the amount of large air pockets trapped along the edges and corners of a hardened particle. Those particles for which air was trapped inside during molding were discarded at a later stage. A glass stirrer bar was used to aid in pouring the mixture from the beaker to the mold. After the molds were filled, they were leveled by scraping the stirrer bar across the top of the mold. This leveling process occasionally created a vacuum resulting in a depression on the surface of the particles. Particles with severe depressions were not used for testing. After the mixture was poured into the molds, it was left to cool to room temperature before being demolded and sanded to remove any jagged edges.

Alternatives to the pouring method were explored, such as baking the slurry in the oven (figure 4.2a) and using a syringe to transfer the cooked slurry from the beaker to the molds (figure 4.2b). Neither of these methods proved successful. When baking, the mixture bubbled over the edges of the mold and what was left on the inside was hollow and grainy. It was not possible to demold these particles and the whole structure crumbled upon contact. The syringe method was not successful due to the quickly setting nature of the cooked slurry. Before the mixture could be successfully molded it hardened within the syringe.

Rod- and disc- shaped particles each had their individual molding challenges. The majority of the disc-like particles did not trap air pockets within them, but the mixture often did not flow all the way to the corners of the mold cavity, leaving the edges of the particles rounder than the intended shape. For the rod-like particles, the corners presented less of a problem. However, on average there were more rod-like particles that contained hidden
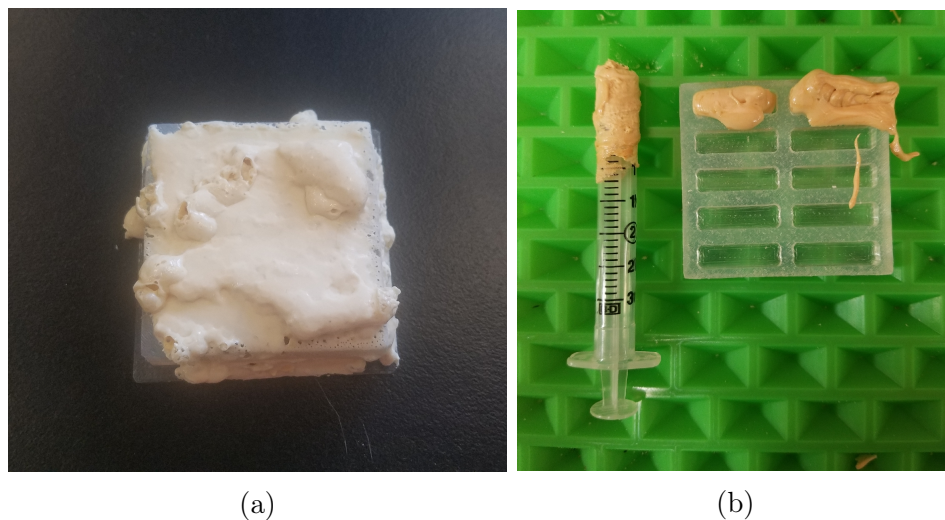
(a) (b)

Figure 4.2: Two different ways of molding particles. (a) Shows attempts at baking the slurry directly in the molds. (b) Shows attempts at using a syringe to transport the cooked slurry from the beaker to the molds.
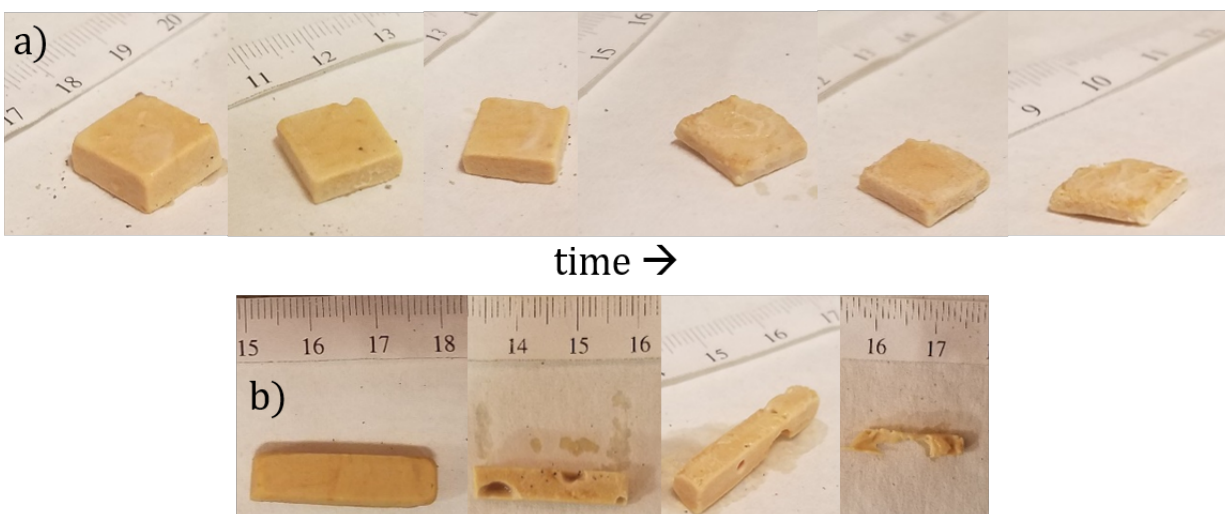

time →

Figure 4.3: a) Shows an example disc-like particle as it dissolves. b) Shows a dissolving rod-like particle with trapped air bubbles.

air pockets than disc-like particles. An example of this can be seen in figure 4.3, where the rod-like particle dissolved irregularly due to the hollow cavities. The cavity inside the particle did not become apparent until the particle started to dissolve. When cavities appeared, the particle and the data were discarded and the experiment was repeated with a new particle. Some batches of particles had more air pockets in them than others, depending on how quickly the mixture was poured into the molds after reaching the ideal temperature. The results presented here include only particles that maintained their shape as they were tested.

Verification of Material Properties

Numerous verification and classification methods of material properties were explored. One such property was a hardness characterization attempted using a Rockwell Hardness tester. Unfortunately, the initial load provided enough force to shatter the particles, therefore not allowing for a reading from this instrument. Using the Mohs Hardness Test Dr. Michael Riemer and Dr. Nicholas Sitar found that the particle had a Mohs Hardness rating of 2, the same hardness as gypsum.

Thermogravimetric analysis (TGA) was performed to determine how consistent particles were across batches. The TGA tests were performed only on a few samples and showed water concentrations of 2.74%, 2.87%, and 2.56% , which were approximately 2.2 percentage points lower than our measured water content for the corresponding batches. Additionally, both the TGA and direct water content measurements were very consistent and showed little variation in water content between the different particle batches. The mean directly measured water content for all of the batches was $5.7\% \pm 0.2\%$. Differential scanning calorimetry was also considered as a way to measure water content, but this method was not compatible with the particle composition.

As surface area was suspected to play a role in the dissolution rate of the particles, characterization of the surface roughness was attempted. Particles were imaged using a borescope magnification set-up. The particles before and after dissolving showed similar surface roughness when being magnified by the borescope and inspected by eye. The images taken through the borescope showed the same results. Microscopy images were also attempted, but the composition of the particles once again made this technique unfeasible given the tools available for use.

4.3 Discussion

The method described in Section 4.2 fulfilled our goal to find a pourable recipe that creates particles capable of holding their shape as they dissolve. However, there were some limitations regarding the shelf-life of the particles and their moldability. The shelf-life, or how long a certain batch of particles can be stored, depends on particle moisture content and the relative humidity both on the day the particles were made and during particle storage.
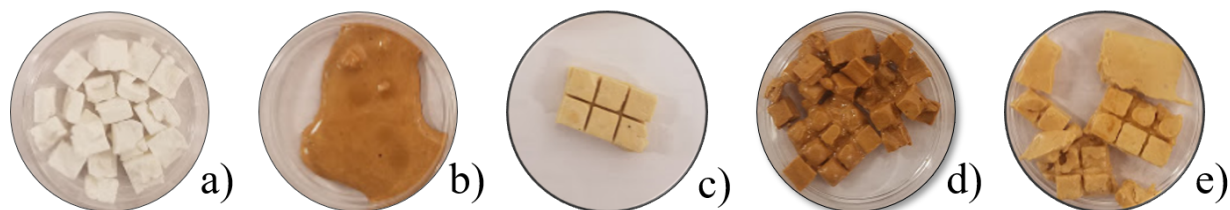
Figure 4.4: Results from recipe trials. The dextrose-to-sucrose ratio is increasing from sample a) to sample e). a) no dextrose, low-temp; b) no dextrose, high-temp; c) low dextrose-to-sucrose ratio, mid-temp; d) low dextrose-to-sucrose ratio, high-temp; e) high dextrose-to-sucrose ratio, mid-temp. The side-length of each of the cubes pictured is 7.5mm.

In certain situations, the particles may become sticky during storage and start to "weep," i.e. lose their structure and have a fluctuating water content Ergun, Lietha, and R. W. Hartel 2010. Fluctuating water content is a result of the water activity in a particle and causes structural instability, shortening the allowable storage time between manufacturing and testing.

The particles typically start with low water activity, indicating little water in the particle is available to contribute to physical or chemical processes Ergun, Lietha, and R. W. Hartel 2010. This leads to the movement of moisture from the air to the particle surface. To visualize this, imagine finding a piece of old candy in the back of the pantry. Old candy tends to be sticky and difficult to separate from its wrapper Richard W. Hartel, Elbe, and Hofberger 2018. The old candy has increased in water content as it gains water molecules from the air around it, making it sticky. Exchange of water molecules between air and particles is not one-directional nor is the water concentration in each medium often at equilibrium. Once the surface of the particles (or candy) starts accepting water, the total water activity of the particles will increase. As a result of the increased water activity, more water will move from the particle to the air than from the air to the particle (a net loss in water). Since the particle now has fewer water molecules than the air, it will start accepting water molecules again. The trading of water molecules from the air to the particles and back again leads to disintegration of the particles, and causes them to become soft, sticky, and lose their shape Ergun, Lietha, and R. W. Hartel 2010. Figure 4.4b and 4.4d show examples of weeping particles; figure 4.4a and 4.4e show incompletely molded particles; figure 4.4c is the final recipe used.

The temperature of the recipe during cooking strongly influences the final water content of a particle as well. A batch cooked too long will have a very low water content, and therefore low water activity. The lower the water activity is, the more rapidly water will move from the atmosphere to the particle as a result of a steeper concentration gradient. The higher gradient leads to faster decomposition of the shape and a shorter amount of time the particle can be stored before it is tested. Arriving at the ideal water content and temperature combination also influences how well the molds can be filled and leveled off. In our effort to find a procedure reliable enough for scientific study, we tested over 100 batches varying

recipes and methods of mixing and molding. In terms of molding, we found pouring to be the best method (see figure 4.2). Small fluctuations in the initial mass of a particle were not uncommon as a result of small variations in particle manufacturing. Slight departures from neutral buoyancy are visually obvious to the experimenter. Our recipe using 5.55g of bubbles stays suspended in the water tank, while the one with 5.60g and 5.50g go directly to the top or bottom of the tank and stay there.

Although the rod- and disc- shaped particles became skinnier and flatter as they dissolved, they still maintained their 'rod' and 'disc' form. Evidence of this shape-similarity is shown in figure 4.3. The dissolving rod-like particles were more fragile than the disc-like particles, but they generally did not break due to handling or fluid motion unless they contained air bubbles resulting from poor manufacturing (evidence of this shown in figure 4.3b). Both types of particles held their shape until they were too small to accurately register on the weighing scale at our disposal. This success was predicated on following the appropriate recipe and achieving the correct temperature and water content (figure 4.4c).

4.4 Conclusion

In this chapter, I presented an alternative to the gypsum-dissolution method for measuring mass transfer in turbulent flow. I demonstrated a successful recipe for a neutrally buoyant mixture of sugar and hollow glass spheres and a method for molding the recipe into disc- and rod- shaped particles. To maximize particle yield, accurate water content and temperature measurements were vital and ensured optimal particle composition. While I encountered challenges with molding the particles and maximizing their shelf life, I found the presented method to be successful.

Acknowledgements

References

Angradi, Ted and Robert Hood (1998). "An application of the plaster dissolution method for quantifying water velocity in the shallow hyporheic zone of an Appalachian stream system". en. In: *Freshwater Biology* 39.2, pp. 301–315. ISSN: 1365-2427. DOI: 10.1046/j.1365-2427.1998.00280.x.

Bagøien, Espen and Thomas Kiørboe (2005). "Blind dating—mate finding in planktonic copepods. I. Tracking the pheromone trail of Centropages typicus". en. In: *Marine Ecology Progress Series* 300, pp. 105–115. ISSN: 0171-8630, 1616-1599. DOI: 10.3354/meps300105.

Baird, M. E. and M. J. Atkinson (1997). "Measurement and prediction of mass transfer to experimental coral reef communities". en. In: *Limnology and Oceanography* 42.8, pp. 1685–1693. ISSN: 1939-5590. DOI: 10.4319/lo.1997.42.8.1685.

Bird, R. Byron, Warren E. Stewart, and Edwin N. Lightfoot (2007). *Transport phenomena*. Rev. 2nd ed. J. Wiley. ISBN: 978-0-470-11539-8.

Boon-Long, S., C. Laguerie, and J. P. Couderc (1978). "Mass transfer from suspended solids to a liquid in agitated vessels". en. In: *Chemical Engineering Science* 33.7, pp. 813–819. ISSN: 0009-2509. DOI: 10.1016/0009-2509(78)85170-7.

Chang, Sandy, Chris Elkins, John K. Eaton, and Stephen Monismith (2013). "Local mass transfer measurements for corals and other complex geometries using gypsum dissolution". en. In: *Experiments in Fluids* 54.7, p. 1563. ISSN: 1432-1114. DOI: 10.1007/s00348-013-1563-x.

Ergun, R., R. Lietha, and R. W. Hartel (2010). "Moisture and Shelf Life in Sugar Confections". In: *Critical Reviews in Food Science and Nutrition* 50.2, pp. 162–192. ISSN: 1040-8398. DOI: 10.1080/10408390802248833.

Feng, Pan, Alexander S. Brand, Lei Chen, and Jeffrey W. Bullard (2017). "In situ nanoscale observations of gypsum dissolution by digital holographic microscopy". In: *Chemical Geology* 460, pp. 25–36. ISSN: 0009-2541. DOI: 10.1016/j.chemgeo.2017.04.008.

Grijseels, H., D. J. A. Crommelin, and C. J. de Blaey (1981). "Hydrodynamic approach to dissolution rate". en. In: *Pharmaceutisch weekblad* 3.1, pp. 1005–1020. ISSN: 0031-6911, 1573-739X. DOI: 10.1007/BF02193318.

Hartel, Richard W., Joachim H. von Elbe, and Randy Hofberger (2018). *Confectionery Science and Technology*. en. Springer International Publishing. ISBN: 978-3-319-61740-4.

Huang, Jinzi Mac, M. Nicholas J. Moore, and Leif Ristroph (2015). "Shape dynamics and scaling laws for a body dissolving in fluid flow". In: *Journal of Fluid Mechanics* 765. ISSN: 0022-1120, 1469-7645. DOI: 10.1017/jfm.2014.718.

Kiørboe, Thomas, Hans-Peter Grossart, Helle Ploug, and Kam Tang (2002). "Mechanisms and Rates of Bacterial Colonization of Sinking Aggregates". en. In: *Applied and Environmental Microbiology* 68.8, pp. 3996–4006. ISSN: 0099-2240, 1098-5336. DOI: 10.1128/AEM.68.8.3996-4006.2002.

Levins, D. M. and J. R. Glastonbury (1972). "Application of Kolmogorofff's theory to particle—liquid mass transfer in agitated vessels". en. In: *Chemical Engineering Science* 27.3, pp. 537–543. ISSN: 0009-2509. DOI: 10.1016/0009-2509(72)87009-X.

Machicoane, N., J. Bonaventure, and R. Volk (2013). "Melting dynamics of large ice balls in a turbulent swirling flow". In: *Physics of Fluids* 25.12, p. 125101. ISSN: 10706631. DOI: 10.1063/1.4832515.

Nazaroff, W. W. and Lisa Alvarez-Cohen (2001). *Environmental engineering science*. Wiley. ISBN: 0-471-14494-0.

Pachon-Rodriguez, Edgar Alejandro and Jean Colombani (2013). "Pure dissolution kinetics of anhydrite and gypsum in inhibiting aqueous salt solutions". en. In: *AIChE Journal* 59.5, pp. 1622–1626. ISSN: 1547-5905. DOI: 10.1002/aic.13922.

Porter, Elka T., Lawrence P. Sanford, and Steven E. Suttles (2000). "Gypsum dissolution is not a universal integrator of 'water motion'". en. In: *Limnology and Oceanography* 45.1, pp. 145–158. ISSN: 1939-5590. DOI: 10.4319/lo.2000.45.1.0145.

Sano, Yuji, Nobutaka Yamaguchi, and Toshiro Adachi (1974). "Mass Transfer Coefficients for Suspended Particles in Agitated Vessels and Bubble Columns". In: *Journal of Chemical Engineering of Japan* 7.4, pp. 255–261. DOI: 10.1252/jcej.7.255.

Sasson, Daniel A., Anya A. Jacquez, and Joseph F. Ryan (2018). "The ctenophore Mnemiopsis leidyi regulates egg production via conspecific communication". In: *BMC Ecology* 18.1, p. 12. ISSN: 1472-6785. DOI: 10.1186/s12898-018-0169-9.

Stocker, Roman, Justin R. Seymour, Azadeh Samadani, Dana E. Hunt, and Martin F. Polz (2008). "Rapid chemotactic response enables marine bacteria to exploit ephemeral microscale nutrient patches". en. In: *Proceedings of the National Academy of Sciences* 105.11, pp. 4209–4214. ISSN: 0027-8424, 1091-6490. DOI: 10.1073/pnas.0709765105.

Thompson, T. Lewis and Edward P. Glenn (1994). "Plaster Standards to Measure Water Motion". In: *Limnology and Oceanography* 39.7, pp. 1768–1779. ISSN: 0024-3590.

Chapter 5

Effects of Form on Dissolution

5.1 Introduction

Particle motion within the intertial subrange of turbulence is an open question due to the complexities of competing forces. The inertial subrange contains the scales of turbulence which have a nearly constant rate of energy transfer from large scales to small scales without significant energy loss due to viscosity. Particles whose size are in the inertial subrange of turbulence are influenced by unsteady fluid forcing (from the turbulent flow), by the boundary layer surrounding the particle and flow separation, and by inertia from the particle mass. This is an interesting regime in which particles are large enough to inertially cross fluid streamlines, yet small enough to be moved by turbulent fluctuations. In addition to size, we consider shape as an important feature because shape and size work together to determine how a particle reacts to ambient turbulent forcing Bordoloi and E. Variano 2017. The influence of shape on rotation has recently become the subject of investigation Voth and Soldati 2017; Pujara, Oehmke, et al. 2018; Oehmke, Bordoloi, et al. 2021 and rotation likely influences mass transfer.

Particles smaller than the Kolmogorov scale, the smallest lengthscale of turbulence, move with a Stokesian response to a time-varying linear shear flow. Simulations of this motion in homogeneous, isotropic turbulence demonstrate differences in the ways rods and discs move M. Byron et al. 2015; Parsa and Voth 2014; Chevillard and Meneveau 2013; Pujara, Voth, and E. A. Variano 2019. Rods tend to spin (rotate around their symmetry axis) while discs have a tendency to tumble (rotation of the symmetry axis) M. Byron et al. 2015. Chapter 3 discusses whether the tendency of a certain shape towards tumbling versus spinning persists for particles in the inertial subrange.

An additional layer of complexity is added when considering both mass and momentum boundary layers. Previous work by Haugen et al. (2017) on mass transfer in turbulent suspensions of sub-Kolmogorov-scale particles used extensions of point-particle methods, which makes the assumption that the particles are smaller than the smallest scales of the flow Balachandar and Eaton 2010. For mass transfer dynamics, direct numerical simulations
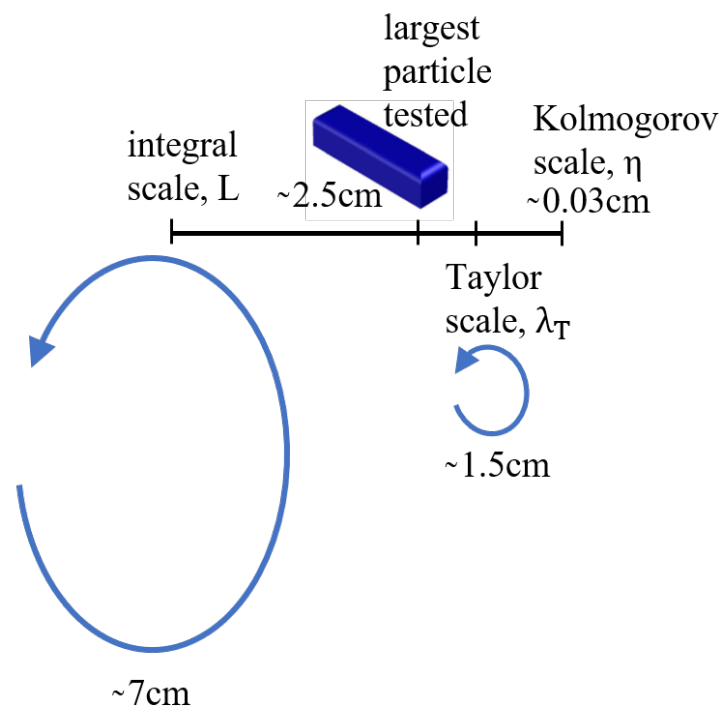
Figure 5.1: This scale bar shows the important turbulent lengthscales from the Kolmogorov scale to the integral scale. The largest particle that is tested, the Vrod, has a length of 2.5cm and is slightly larger than the Taylor scale.

(DNS) of particles using the point-particle approximations completely resolve all sales of the ambient turbulence and the additional scales introduced by the particles. Using the point-particle approach fails when particles are larger than the Kolmogorov scale, but smaller than the energy-containing scales that begin the turbulent 'cascade.' A scale in between those two extremes is the Taylor lengthscale Pope 2000. Our particles, being near the Taylor scale (see figure 5.1), experience both fluid viscous forces and particle inertial forces at non-negligible magnitudes. To understand how particles at the Taylor scale interact with turbulence requires resolving the unsteady particle boundary layer as part of turbulent DNS Cisse, Homann, and Bec 2013; Voth 2015; Fornari et al. 2016; Do-Quang et al. 2014; Lucci, Ferrante, and Elghobashi 2010; Uhlmann 2008. However, DNS is not yet practical for looking at mass transfer across the fluid-particle interface due to the costly extra grid resolution needed to resolve scalar fields down to the smallest scale of mass transport, the Batchelor scale. Therefore, laboratory methods are currently the most practical means by which to measure mass transfer rate of Taylor-scale-sized particles in turbulent flow.

Studies by Huang, Moore, and Ristroph (2015) have taken a similar approach of using dissolution to characterize water motion coupled with shape dynamics. In these experiments, hard candies (instead of gypsum) were dissolved in laminar high-speed flows to study the

evolution of particle shape and the receding candy surface. This process showed shape convergence of cylinders and hemispheres to a steady terminal form Huang, Moore, and Ristroph 2015. The overall dissolution rate of the sugar increased with the square root of flow speed, and the volume of the submerged body vanished quadratically in time. Due to the shape-flow feedback, this experiment resulted in a moving boundary layer problem Huang, Moore, and Ristroph 2015. Using scaling laws, Huang, Moore, and Ristroph (2015) were able to find a recession velocity based only on relevant scales such as diffusivity and boundary layer thickness. Their experiments show evolution of a solid body towards a state of uniform shear and therefore uniform material flux Huang, Moore, and Ristroph 2015. While these experiments could hold insights into the behavior of freely-moving sugar particles, their experiments were performed in laminar flow and simplified to a 2D model. Turbulence, on the other-hand, is inherently 3D and unsteady.

In this chapter I will use our custom particles (see ch. 4) to investigate the dissolution rate of dissolving particles in turbulent flow. Defining the shape-motion-flux relationship will help clarify fundamental questions about particle-turbulence interactions within the inertial subrange.

5.2   Methods

I tested three different cuboid particles whose shapes traversed the surface-area-aspect-ratio-volume domain of interest. Two different 'rods' were tested in this experiment and one 'disc'. The discs had dimensions of 12.7mm x 12.7mm x 6.35mm and an aspect ratio (aspect ratio = symmetry axis length : degenerate axis length) of 0.5. The first rod was matched by volume to the disc, and is therefore named Vrod. The Vrod had dimensions of 6.35mm x 6.35mm x 25.4mm and an aspect ratio of 4. A disc and Vrod example can be seen in figure 5.2. The second rod was matched by aspect ratio to the Vrod and matched by surface area to the disc. This rod was named Srod and had dimensions of 5.98mm x 5.98mm x 23.95mm. The Srod is not pictured in figure 5.2, but it does look very similar to the Vrod.

Volume-matched particles were chosen because studies show that particle volume, and not surface area or aspect ratio, control the rotation of Taylor-scale-sized particles suspended in isotropic turbulence Bordoloi and E. Variano 2017; M. Byron et al. 2015. In chapter 3 we saw that the size of the particle determined its spinning and tumbling rate, not the shape. Because rotation and mass transfer both depend on fluid shear near the particle surface, we take rotation as an initial prediction of mass transfer behavior.

Characterization of the dissolution rate for the particles was performed in a homogeneous, isotropic turbulence tank. The turbulence tank described in Bellani and E. A. Variano (2014) was used to evaluate the shape dependence of the mass transfer rate. The test section of the tank is 80cm x 80cm x 75cm and is located in the middle of the tank between two mesh screens. The screens were used to prevent particles from going into the jet intake. Turbulence in the tank was created by two 8x8 arrays of synthetic jets, located at opposite ends of the tank, and positioned to face each other. The jets were randomly actuated in
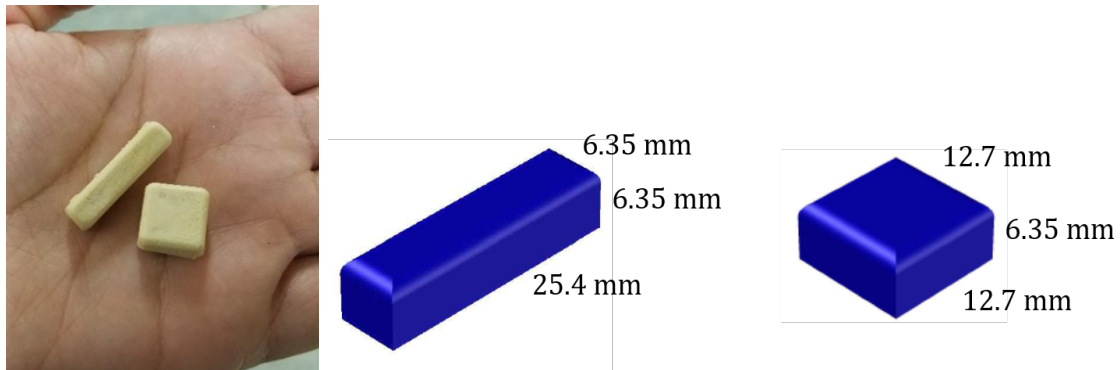
Figure 5.2: Neutrally buoyant dissolving particles using our new manufacturing method. Rod-shaped particles are shown on the left and disc-shaped particles are shown on the right. The rod-shaped particles pictured are matched by volume to the disc-shaped particles.
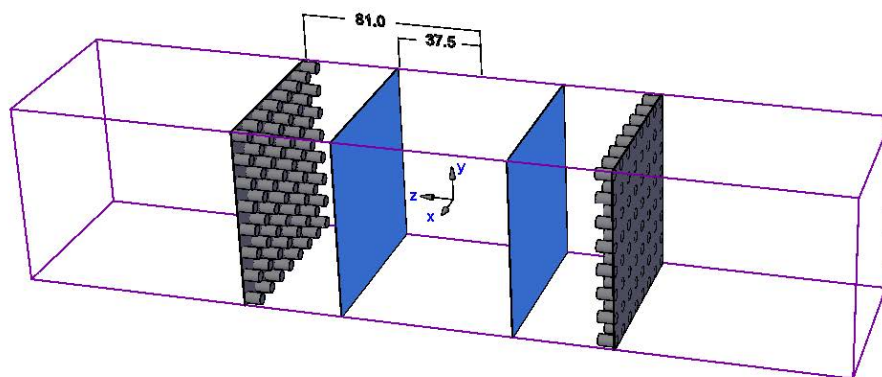

Figure 5.3: Turbulence tank used to evaluate sugar-glass-sphere particles. The screens were placed in the tank to enhance flow isotropy and to keep the particles from coming into contact with the jet arrays. Units in the diagram are in centimeters. The entire length of the tank is 360cm and the cross section is 80cm by 80cm.

a way to maximize isotropy and minimize mean flow Bellani and E. A. Variano 2014. The turbulence tank was filled with filtered and degassed tap water. A schematic of the tank is shown in Figure 5.3.

Turbulent quantities were taken from Margaret Byron (2015) and Bellani, Nole, and E. A. Variano (2013) and averaged over the entire volume of the test section. The volume-averaged energy dissipation rate was $5.49 \times 10^{-5} \mathrm{m}^2/\mathrm{s}^3$, the volume-averaged turbulent velocity (u_{rms}) was $1.98 \times 10^{-2}\mathrm{m/s}$, and the volume-averaged Taylor scale was $\lambda_\tau = 1.55 \times 10^{-2}\mathrm{m}$. The proposed characteristic scale of interest for particle dynamics is the diameter of a sphere with the same volume as that of our particles. This sphere-equivalent diameter, d_{eq}, can be non-dimensionalized using the Taylor scale: $d_{eq}* = d_{eq}/\lambda_\tau = 0.81$. In following the method used by Machicoane, Bonaventure, and Volk (2013), we calculate a mixed Reynolds number $u_{rms} * d_{eq}/\nu = 247$. We do not vary the turbulence intensity in this study, so comparisons between turbulent forcing and mass transfer rates are not included.

The mass transfer rate of the shapes was characterized by taking measurements of the mass of a single particle until it had completely dissolved. This was repeated one-by-one for each rod- and disc- shaped particle that was tested. Each particle was dropped into the tank while the jets were firing, and then was removed from the tank after 60-80 seconds using an aquarium fish net. Kimwipes® were used to prevent the particles from sticking to the scale. Once the wipe was placed on the scale, the scale was tared and the mass of the particle was measured. The mass of the particle and the amount of time it spent in the tank were recorded. After the measurements were taken, the particle was placed back in the tank so it could continue to interact with the flow. The process of removing the particle, recording the time, and recording its mass, was repeated until the particle was too small to register on the scale (less than 0.1g). The presented data show the results of the two shapes that were tested. This experiment was repeated multiple times to check repeatability. Presented here are the results for approximately 10 particles for each of the three shapes. The data is different that what is published in Oehmke and E. A. Variano 2021 due a change in the base-materials received from the suppliers which lead to a change in the particle recipe.

The neutrally buoyant particles do get stalled at boundaries, and can spend anywhere from about 2 seconds to 2 minutes there. They always leave the boundary, and the majority of time is spent in the tank and not at boundaries. Particle behavior appears to be the same at each of the boundary types (one free-slip surface, one no-slip bottom, two no-slip walls, and two porous walls). Figure 5.4 shows a short time-lapse (6 seconds at 1-second intervals) of particle motion. At the beginning of the time-lapse, the particle moved 2-3 times its length in 1 second. At the end of the time-lapse, the particle was almost stationary for several seconds. The particle was not near the boundaries when these images were taken.

5.3 Analysis and Results

Figure 5.5a shows the particle mass as it dissolves over time and a model fitted to each of the three particle forms. The mass flux away from the particle is greater at early times, i.e.
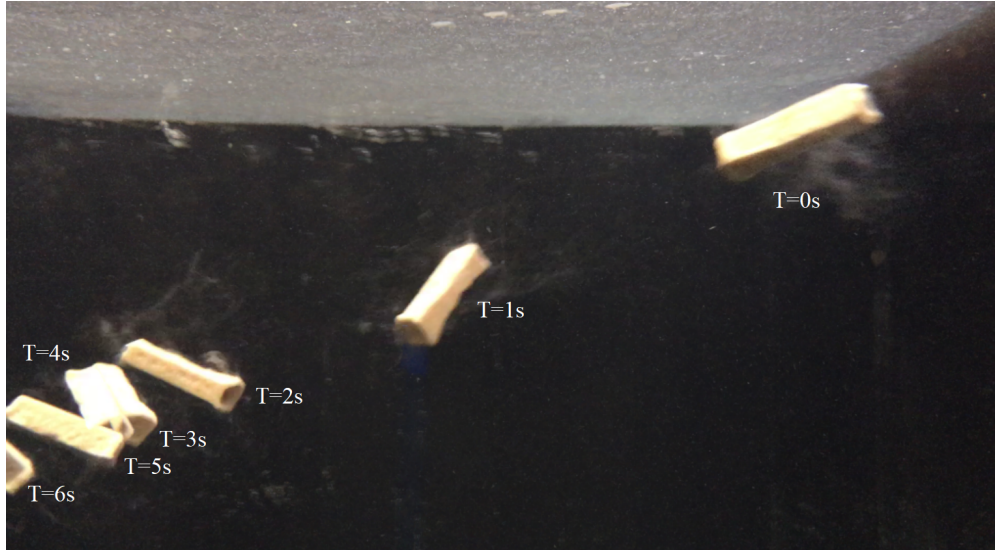
Figure 5.4: Time-lapse of particles suspended in turbulence tank. These images cover 6 seconds of particle motion. At the beginning the particle had a downward trajectory due to the momentum from being dropped in the tank. After around 2 seconds, the particle starts to rotate in space at approximately a constant location.

when the particle is larger as represented by the steeper slope. This is no surprise, given that surface area is larger at early times. A classic model for dissolution that is based only on geometry is the Hixson-Crowell model Hixson and Crowell 1931. It assumes that mass flux away from the surface is a constant, and that the geometry is simple enough that particle lengths decrease linearly with time.

Inspired by the Hixson-Crowell model, we assume that mass is lost normal to the surface at a constant rate k [$length/time$], and that all sides recede a length kt in a direction normal to the surface. Implicit in this formulation is the fact that the dissolution rate is not influenced by the accumulation of solute in the ambient fluid nor in the boundary layer close to the particle. This method has a small bias in how it handles the corners of objects, but the spread in our data suggests that it is not worth proceeding to more advanced models that integrate local fluxes around the surface.

Our model is shown in equation 5.1. Here l_0, w_0, and h_0 are the initial length, width, and height of the particles, respectively. V_t is the particle volume at a given time, t. We assume that density is constant, so volume and mass are linearly related.

$$V_t = (l_0 - kt)(w_0 - kt)(h_0 - kt) \tag{5.1}$$

The presented data in figure 5.5a exhibits a trend in agreement with the proposed model. In this model, we assume that the mass flux is constant for a particle freely suspended in turbulence. Results from Machicoane, Bonaventure, and Volk (2013) provide support for this assumption.

Table 5.1: Dissolution rate, k, as measured for rod- and disc- shaped particles. These values were calculated using the model presented in Equation 5.1 and shown in Figure 5.5.

Particle type	surface area, SA [cm^2]	volume, V [cm^3]	SA:V [1/cm]	dissolution rate, k [cm/min]	95% conf. interval [cm/min]	R^2 value [–]
Disc	6.45	1.02	6.30	0.041	[0.040 0.042]	0.984
S-Rod	6.44	0.86	7.52	0.039	[0.039 0.041]	0.968
V-Rod	7.26	1.02	7.09	0.036	[0.035 0.038]	0.938
Extrap. Rod	–	–	6.30	0.031	–	–

The model in equation 5.1 was fitted to the data in figure 5.5 by using Matlab's 'fit' function and defining our 'fitType' (created with Matlab's 'fittype' function) as equation 5.1. The single fit parameter is the dissolution rate, k. Table 5.1 summarizes the important calculated values including the 95% confidence interval for the dissolution rates.

Turbulence is one of several effects that are grouped into a single factor k. We cannot predict k *a priori*, but the new method presented herein provides a potential route to assembling a large enough dataset of dissolution rates that one could connect k to the dynamics of the unsteady boundary layer on suspended particles.

Figure 5.5b highlights the different dissolution rates by using a representative data point for each of the three particles. Presented in figure 5.5b is one symbol per time per type of particle. The error bars indicate the scatter in the particle mass due to repeated measurements. The error associated with the time a measurement was taken is also presented, but this error is not visible for the most part as the standard error in the time measurements was less than 2.5 seconds.

The data is this dissertation are newer than the data in the published article Oehmke and E. A. Variano 2021, although the analysis methods are the same.

5.4 Discussion

In the proposed model, predicting k *a priori* is challenging because it combines turbulence and material properties into a single value. Nevertheless, the data from our experiments seem to fit this model relatively well. In figure 5.5 the discs are plotted as blue circles, the Vrods as yellow downward-pointing triangles and the Srods as red diamonds. The three fit lines for each of the different shapes is plotted as well, with blue dashed, yellow solid, and red dashed referring to discs, Vrods, and Srods respectively.

From the results so far when comparing the disc-like and rod-like particles, I've seen that while holding volume constant the discs dissolve faster at a 95% confidence level. When holding the surface area constant, the discs dissolve faster at a confidence level slightly
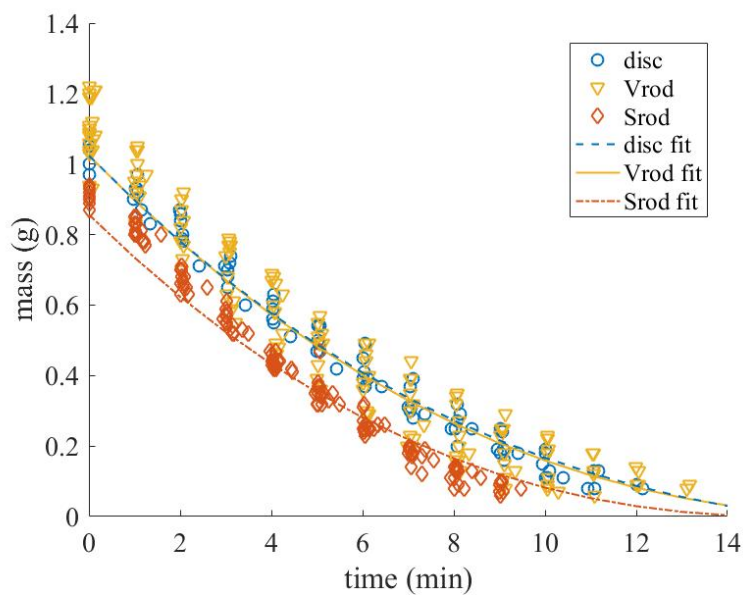
(a)
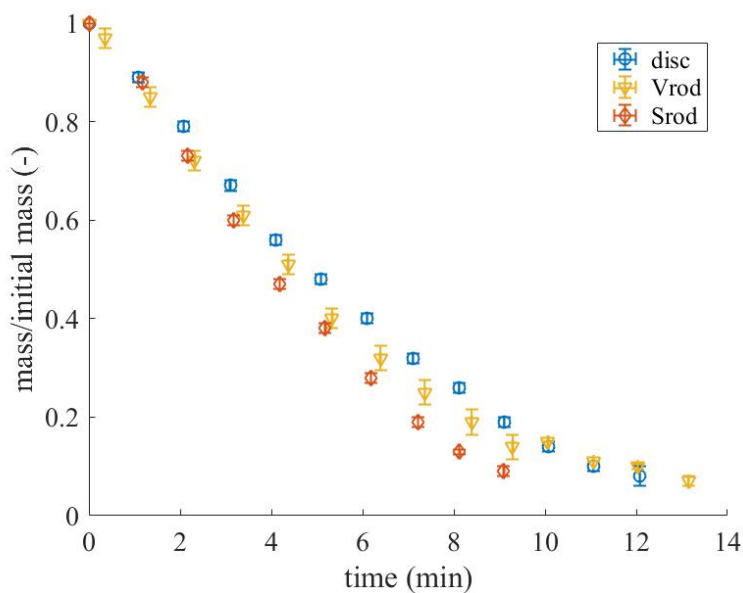
(b)

Figure 5.5:   Results of the mass transfer experiments. a) Shows the fit of the data to the model. Each trajectory is a single particle and vertical variation is due to individual particle idiosyncrasy. b) Plots mean mass and time for each measurement cluster. Mass is normalized by initial mass for an individual particle. The error bars represent the scatter in the data due to repeated measurements. Blue circles represent discs, yellow triangles represent Vrods, and red diamonds represent Srods.

below 95%. And then holding the specific surface constant, the discs dissolve faster at a 95% confidence level.

From figure 5.5, Vrods overall took the longest time to dissolve, which can be seen by the tail of the data extending out the farthest to the right. The disc and Vrod data does overlap quite a bit, but overall the discs were the quickest to dissolve (see table 5.1). Even though the Srods started out the smallest (as a factor of design), they did not dissolve the quickest out of all three shapes. The Srod dissolution rate was solidly in the middle of the other two shapes, and the dissolution rate value for Srods is only statistically separate from the discs at less than a 95% confidence interval.

One reason Vrod- and disc- like particles have different dissolution rates could be due to the difference in aspect ratios which cause particles to sample the turbulence in a biased manner M. Byron et al. 2015. To test this, I compared the Vrod and Srod particles. Although these two particles have the same aspect ratio, they have dissolution rates that are statistically different from each other at the 95% confidence level.

Another reason for the different dissolution rates in volume-matched particles could be due to the difference in their specific surfaces (surface-area-to-volume ratios). Although this was not tested explicitly, this data can be extrapolated from the results in table 5.1. Using a linear extrapolation from the two measured rod-like particles, we obtain the predicted dissolution rate for a rod-like particle with a specific surface of 6.3 cm^{-1} (the specific surface of the dis particle measured herein). The extrapolated dissolution rate is 0.031 cm/min which is much smaller than the dissolution rate for the disc, measured as 0.041 cm/min.

Future work using the technique presented herein will be able to cover a large enough parameter space to fit a model that parses out the different effects of shape, size, turbulence intensity, etc. For example, a model would ideally include factors for the turbulent boundary layer thickness around the particle, the dissolution rate of the particle in laminar flow, and shape effects. I would like to separate out the effect of factors such as aspect ratio, edge length, and corners and protrusions, as well as particle kinematics in turbulence, e.g. rods experiencing more 'angular slip' or sweeping out broader volumes of space as they rotate. For now, we have chosen a one-parameter model because it matches the amount of data I have.

5.5 Conclusion

From the experiments I performed, I found that the data followed the proposed dissolution model and that disc-shaped particles had a slightly faster dissolution rate compared to both rod-shaped particles. Surface area, volume, and surface-area-to-volume ratio have all been compared between the two different forms, discs and rods, and the disc-like particles dissolved faster in all cases when the parameters of interest were comparable.

Determining particle-specific dissolution rate parameters is important for understanding the shape-motion-flux relationships of dissolving objects. Additional experiments should be performed where both the surface area and the mass are recorded at each time interval.

More shapes, surface-area-to-volume ratios, and aspect ratios should also be tested along with varying the turbulence intensity to explore how the dissolution relates to d_{eq}, surface area, volume, and turbulence.

Acknowledgements

References

Balachandar, S. and John K. Eaton (2010). "Turbulent Dispersed Multiphase Flow". In: *Annual Review of Fluid Mechanics* 42.1, pp. 111–133. DOI: 10.1146/annurev.fluid.010908.165243.

Bellani, Gabriele, Michael A. Nole, and Evan A. Variano (2013). "Turbulence modulation by large ellipsoidal particles: concentration effects". en. In: *Acta Mechanica* 224.10, pp. 2291–2299. ISSN: 0001-5970, 1619-6937. DOI: 10.1007/s00707-013-0925-z.

Bellani, Gabriele and Evan A. Variano (2014). "Homogeneity and isotropy in a laboratory turbulent flow". In: *Experiments in Fluids* 55.1. ISSN: 0723-4864, 1432-1114. DOI: 10.1007/s00348-013-1646-8.

Bordoloi, Ankur D. and Evan Variano (2017). "Rotational kinematics of large cylindrical particles in turbulence". en. In: *Journal of Fluid Mechanics* 815, pp. 199–222. ISSN: 0022-1120, 1469-7645. DOI: 10.1017/jfm.2017.38.

Byron, M., J. Einarsson, K. Gustavsson, G. Voth, B. Mehlig, and E. Variano (2015). "Shape-dependence of particle rotation in isotropic turbulence". en. In: *Physics of Fluids* 27.3, p. 035101. ISSN: 1070-6631, 1089-7666. DOI: 10.1063/1.4913501.

Byron, Margaret (2015). "The rotation and translation of non-spherical particles in homogeneous isotropic turbulence". English. Ph.D. University of California, Berkeley.

Chevillard, Laurent and Charles Meneveau (2013). "Orientation dynamics of small, triaxial–ellipsoidal particles in isotropic turbulence". en. In: *Journal of Fluid Mechanics* 737, pp. 571–596. ISSN: 0022-1120, 1469-7645. DOI: 10.1017/jfm.2013.580.

Cisse, Mamadou, Holger Homann, and Jeremie Bec (2013). "Slipping motion of large neutrally-buoyant particles in turbulence". In: *Journal of Fluid Mechanics* 735. ISSN: 0022-1120, 1469-7645. DOI: 10.1017/jfm.2013.490.

Fornari, W., A. Formenti, F. Picano, and L. Brandt (2016). "The effect of particle density in turbulent channel flow laden with finite size particles in semi-dilute conditions". In: *Physics of Fluids* 28.3, p. 033301. ISSN: 1070-6631. DOI: 10.1063/1.4942518.

Haugen, Nils Erland L., Jonas Kruger, Dhrubaditya Mitra, and Terese Løvås (2017). "The effect of turbulence on mass and heat transfer rates of small inertial particles". In: *arXiv:1701.04567 [physics]*.

Hixson, A. W. and J. H. Crowell (1931). "Dependence of Reaction Velocity upon surface and Agitation". In: *Industrial & Engineering Chemistry* 23.8, pp. 923–931. ISSN: 0019-7866. DOI: 10.1021/ie50260a018.

Huang, Jinzi Mac, M. Nicholas J. Moore, and Leif Ristroph (2015). "Shape dynamics and scaling laws for a body dissolving in fluid flow". In: *Journal of Fluid Mechanics* 765. ISSN: 0022-1120, 1469-7645. DOI: 10.1017/jfm.2014.718.

Lucci, Francesco, Antonino Ferrante, and Said Elghobashi (2010). "Modulation of isotropic turbulence by particles of Taylor length-scale size". en. In: *Journal of Fluid Mechanics* 650, pp. 5–55. ISSN: 1469-7645, 0022-1120. DOI: 10.1017/S0022112009994022.

Machicoane, N., J. Bonaventure, and R. Volk (2013). "Melting dynamics of large ice balls in a turbulent swirling flow". In: *Physics of Fluids* 25.12, p. 125101. ISSN: 10706631. DOI: 10.1063/1.4832515.

Oehmke, Theresa B., Ankur D. Bordoloi, Evan Variano, and Gautier Verhille (2021). "Spinning and tumbling of long fibers in isotropic turbulence". In: *Physical Review Fluids* 6.4, p. 044610. DOI: 10.1103/PhysRevFluids.6.044610.

Oehmke, Theresa B. and Evan A. Variano (2021). "A new particle for measuring mass transfer in turbulence". en. In: *Experiments in Fluids* 62.1, p. 16. ISSN: 1432-1114. DOI: 10.1007/s00348-020-03084-5.

Parsa, Shima and Greg A. Voth (2014). "Inertial Range Scaling in Rotations of Long Rods in Turbulence". In: *Physical Review Letters* 112.2, p. 024501. DOI: 10.1103/PhysRevLett.112.024501.

Pope, Stephen B. (2000). *Turbulent Flows*. Cambridge: Cambridge University Press. ISBN: 978-0-521-59886-6. DOI: 10.1017/CBO9780511840531.

Pujara, Nimish, Theresa B. Oehmke, Ankur D. Bordoloi, and Evan A. Variano (2018). "Rotations of large inertial cubes, cuboids, cones, and cylinders in turbulence". en. In: *Physical Review Fluids* 3.5. ISSN: 2469-990X. DOI: 10.1103/PhysRevFluids.3.054605.

Pujara, Nimish, Greg A. Voth, and Evan A. Variano (2019). "Scale-dependent alignment, tumbling and stretching of slender rods in isotropic turbulence". en. In: *Journal of Fluid Mechanics* 860, pp. 465–486. ISSN: 0022-1120, 1469-7645. DOI: 10.1017/jfm.2018.866.

Do-Quang, M., G. Amberg, G. Brethouwer, and A. V. Johansson (2014). "Simulation of finite-size fibers in turbulent channel flows". In: *Physical Review E* 89.1, p. 013006. DOI: 10.1103/PhysRevE.89.013006.

Uhlmann, Markus (2008). "Interface-resolved direct numerical simulation of vertical particulate channel flow in the turbulent regime". In: *Physics of Fluids* 20.5, p. 053305. ISSN: 1070-6631. DOI: 10.1063/1.2912459.

Voth, Greg A. (2015). "Disks aligned in a turbulent channel". en. In: *Journal of Fluid Mechanics* 772, pp. 1–4. ISSN: 0022-1120, 1469-7645. DOI: 10.1017/jfm.2015.144.

Voth, Greg A. and Alfredo Soldati (2017). "Anisotropic Particles in Turbulence". In: *Annual Review of Fluid Mechanics* 49.1, pp. 249–276. DOI: 10.1146/annurev-fluid-010816-060135.

Chapter 6

Conclusion

In this dissertation I set out to determine how shape and size influence the kinematics and mass flux of Taylor-lengthscale-sized particles in homogeneous isotropic turbulence. From the experiments I conducted, I found that size determined rotation and that disc-like particles dissolve faster than rod-like particles. While similar methods have been used previously to study dissolution, I created a new particle with the important properties of neutral buoyancy and shape-similarity to test dissolution and found that the disc-shaped particles dissolved faster than the rod-shaped particles.

Understanding the dissolution dynamics of the particles tested can also tell us something about their turbulent mass flux $\langle u_i' C' \rangle$. The left-hand side of equation 2.37 can be approximated directly from the experimental measurements that were obtained. The particle change in mass over change in time is known, and from the measured mass we can approximate the surface area that the mass crossed through ($SA \sim (l_0 - kt)^2$).

To find turbulent diffusivity $\mathcal{D}_{turb,i}$, the analysis must go one step farther. Section 5.3 assumes that mass transport is limited by the diffusive boundary layer (rather than the momentum boundary layer) and that the diffusive boundary layer lies within the momentum boundary layer. With these assumptions the $\frac{\partial \langle C \rangle}{\partial x_i}$ term can be approximated as a constant value. Nishihara and Ackerman (2007) describe a way of obtaining an estimate for the boundary layer thickness surrounding a non-moving particle. While the boundary layer would not be the same for a stationary particle and one in turbulence a correction can be applied to account for the different dynamics.

These analyses provide a potential step forward in the challenge of determining and modeling the turbulent mass flux and turbulent diffusivity. While still a rough approximation, this information can help with our understanding of how turbulence influences mixing and transport of solutes when they are released from Taylor-microscale-sized particles. This information is useful in both industrial and natural processes such as pharmaceuticals and oceanic planktonic organism evolution and behavior.

Next steps in this work include looking at particle-particle interactions, understanding how the turbulence surrounding the particle is modulated by particle motion, and turning the collected data into a useful format for environmental turbulence and transport models. More

experiments are necessary for some of these steps, and comparison with numerical models of particle behavior in turbulence is necessary for others. Overall this is an exciting step forward into the realm of rotation dynamics and mass transport with anisotropic, inertial particles.

References

Nishihara, Gregory N. and Josef D. Ackerman (2007). "On the determination of mass transfer in a concentration boundary layer". en. In: *Limnology and Oceanography: Methods* 5.2, pp. 88–96. ISSN: 1541-5856. DOI: https://doi.org/10.4319/lom.2007.5.88.